

ISM Properties in Low-Metallicity Environments

III. The Dust Spectral Energy Distributions of II Zw 40, He 2-10 and NGC 1140

Frédéric Galliano^{1*}, Suzanne C. Madden¹, Anthony P. Jones², Christine D. Wilson³, and Jean-Philippe Bernard⁴

¹ Service d’Astrophysique, CEA/Saclay, L’Orme des Merisiers, 91191 Gif sur Yvette, France

² Institut d’Astrophysique Spatiale (IAS), Université de Paris XI, 91405 Orsay, France

³ Department of Physics and Astronomy, McMaster University, Hamilton, ON L8S 4M1, Canada

⁴ Centre d’Étude Spatiale des Rayonnements (CESR), 31028 Toulouse, France

Received November 16, 2004 / Accepted

Abstract. We present new 450 and 850 μm SCUBA data and 1.3 mm MAMBO data of the dwarf galaxies II Zw 40, He 2-10 and NGC 1140. Additional ISOCAM, IRAS as well as ground based data are used to construct the observed mid-infrared to millimeter spectral energy distribution of these galaxies. These spectral energy distributions are modeled in a self-consistent way, as was achieved with NGC 1569 (Galliano et al. 2003), synthesizing both the global stellar radiation field and the dust emission, with further constraints provided by the photoionisation of the gas. Our study shows that low-metallicity galaxies have very different dust properties compared to the Galaxy. Our main results are: (i) a paucity of PAHs which are likely destroyed by the hard penetrating radiation field, (ii) a very small ($\sim 3-4 \text{ nm}$) average size of grains, consistent with the fragmentation and erosion of dust particles by the numerous shocks, (iii) a significant millimetre excess in the dust spectral energy distribution which can be explained by the presence of ubiquitous very cold dust ($T = 5-9 \text{ K}$) accounting for 40 to 80 % of the total dust mass, probably distributed in small clumps. We derive a range of gas-to-dust mass ratios between 300 and 2000, larger than the Galactic values and dust-to-metals ratios of 1/30 to 1/2. The modeled dust size distributions are used to synthesize an extinction curve for each galaxy. The UV slopes of the extinction curves resemble that observed in some regions in the Large Magellanic Cloud. The 2175 \AA bumps of the modeled extinction curves are weaker than that of the Galaxy, except in the case of II Zw 40 where we are unable to accurately constrain the 2175 \AA bump carrier.

Key words. ISM: dust, extinction – Galaxies: dwarf – Galaxies: starburst – Infrared: galaxies – Submillimeter

1. Introduction

Since dust can either reveal or conceal star formation activity, it plays an important role, often as an elusive villain, in the interpretation of the cosmic star formation history. While characterisation of the detailed dust properties is required to understand the attenuation of the starlight, and to determine the in situ star formation properties, it is difficult to achieve this due to the necessity of sampling a broad range of the dust spectral energy distribution (SED). We have been carrying out studies of detailed SED modeling, with the goal of reproducing a self-consistent model for emission and ex-

tinction in galaxies, in order to explore the effects of different environments on the dust properties. We began our efforts with low metallicity environments. What has been gleaned to date indicates that low metallicity environments can, indeed, harbor non-negligible quantities of dust (Thuan et al. 1999; Plante & Sauvage 2002; Galliano et al. 2003), the effects of which can not be ignored. Additionally, the physical properties of the dust do not resemble those of the Galaxy (Galliano et al. 2003; Vanzi & Sauvage 2004). These results call to question the validity of the seemingly-innocuous assumption of Galactic-dust properties. All of these results have striking implications on the interpretation of extragalactic SEDs, and influence our view of the cosmic star formation history.

Send offprint requests to: galliano@avak.gsfc.nasa.gov

* current address: Infrared Astrophysics Branch, Code 685, NASA Goddard Space Flight Center, Greenbelt, MD 20771, USA

This is the third paper in a series of publications studying the dust properties in star-bursting low-

metallicity dwarf galaxies. The first paper (hereafter paper I; Madden et al. 2005, see Madden 2000, for a preview of this study) was a mid-IR spectroscopic study of a sample of dwarf galaxies observed by ISOCAM. The second paper (Galliano et al. 2003, hereafter paper II) presents a detailed model of the dust SED of the dwarf NGC 1569. Here, we present a study similar to paper II, applied to the three starbursting dwarf galaxies II Zw 40, He 2-10 and NGC 1140. In this paper we pull together all that we have learned from in depth analyses of an assortment of low-metallicity environments.

II Zw 40 is a blue compact dwarf galaxy (BCD), at a distance of $D \simeq 10$ Mpc, often considered to be the prototypical H II galaxy, its nucleus being dominated by one large H II region of ~ 0.5 kpc diameter. Its bright optical core is located inside a large H I envelope. The two tails seen in optical and near-infrared (e.g. Cairós et al. 2001; Vanzi et al. 1996), are the relics of the merger of two smaller galaxies (Brinks & Klein 1988). The starburst could be very young. The metallicity has been determined to be $Z \sim 1/6 Z_{\odot}$ (Masegosa et al. 1994). This galaxy is H I rich ($M(\mathrm{H}\mathrm{I}) = 4.4 \times 10^8 M_{\odot}$; van Zee et al. 1998), while the molecular gas emission is very weak ($M_{\mathrm{mol}} < 0.4 \times 10^6 M_{\odot}$; Meier et al. 2001). The radio continuum emission is compact and mainly thermal free-free (Beck et al. 2002).

He 2-10 (ESO 495-G21) is a very bright southern BCD galaxy, located at a distance of $D \simeq 9$ Mpc. It was the first Wolf-Rayet galaxy to be identified (Allen et al. 1976). Its peculiarities among BCD galaxies is that its metallicity appears to be almost solar (Kobulnicky et al. 1999) and it has a relatively large amount of molecular gas (Meier et al. 2001). The starburst is concentrated in two regions separated by a dust lane. It contains several Super Star Clusters (SSCs) probing a burst of a few Myr (Johnson et al. 2000). This recent burst could have been triggered by the interaction with a molecular cloud (Kobulnicky et al. 1995). A radio map (Kobulnicky & Johnson 1999) reveals several compact thermal continuum sources, indicating ultra-dense H II regions. H α images show a large scale bipolar outflow of gas (Méndez et al. 1999).

NGC 1140 is an amorphous starburst galaxy, larger than II Zw 40 and He 2-10 with a larger reservoir of gas. Its size is roughly $1.7' \times 0.9'$ (Buat et al. 2002), at the distance of $D \simeq 20 - 25$ Mpc. The central H II complex of NGC 1140 has an H α luminosity which is 40 times higher than that of 30 Doradus (Hunter et al. 1994a) and contains several SSCs which have been studied in detail by Hunter et al. (1994b) and de Grijs et al. (2004). Its star formation rate is about $1 M_{\odot} \mathrm{yr}^{-1}$. NGC 1140 may be in the final stages of a merger (Hunter et al. 1994a) and has a small dwarf companion. Among the four dwarf galaxies of our sample (NGC 1569, II Zw 40, He 2-10 and NGC 1140), it is the only one which shows pronounced PAH emission at mid-IR wavelengths (paper I).

The modelling of the global SED of a dwarf galaxy, using actual dust models, has been presented by Madden

(2000), Galliano et al. (2002), Lisenfeld et al. (2002), Galliano et al. (2003), Takeuchi et al. (2003) and this study (see also Galliano 2005). Takeuchi et al. (2003) have used a dust evolution model to fit the IR SED of SBS 0335-052. Lisenfeld et al. (2002) and Galliano et al. (2003) (paper II) applied the Désert et al. (1990) model to NGC 1569. Galliano et al. (2003), having sufficient observational constraints, were able to constrain the dust size distribution of different dust components for NGC 1569. Our conclusion in paper II was that the global IR SED in NGC 1569 is composed of dust components with very different size distributions from our Galaxy and contrary to our Galaxy, is dominated by *small dust particles* ($\lesssim 10$ nm). Additionally, a submillimetre excess was found that could be attributed to a very cold dust component.

Studies on the ISM of dwarf galaxies, on smaller spatial scales have also been conducted. Bot et al. (2004) applied the Désert et al. (1990) model to the diffuse emission of the Small Magellanic Cloud (SMC). While they did not vary the size distribution, they took into account the variations of the radiation field. They had difficulty fitting the $60 \mu\mathrm{m}$ flux. Finally, Plante & Sauvage (2002) and Vanzi & Sauvage (2004) have modelled the dust SED around the SSCs in SBS 0335-052 and NGC 5253, respectively. They used Dusty (Ivezic & Elitzur 1997) which solves the radiative transfer equations in a spherical environment, without considering the process of stochastic heating. In these cases, the size distributions of the local environments were found to be dominated by large grains. These different results obtained for global galactic scales versus more local regions around the SSCs is likely due to the destruction of small grains around SSCs, as is also observed in the vicinity of AGNs (Maiolino et al. 2001a,b).

The paper is organised as follows. Section 2 presents an overview of our new observations and the data we obtained from the literature. Section 4 presents the modeled SEDs of II Zw 40, He 2-10 and NGC 1140 and the consequences of the results on the dust properties. We end with a summary and the conclusions in Sect. 5, which ties together Papers I, II and III.

2. The observations

Observed SEDs were constructed as completely as possible, using our ISOCAM data (paper I), our new 450 and $850 \mu\mathrm{m}$ JCMT (SCUBA) observations and our IRAM (MAMBO) observations presented here, as well as incorporating data from the literature for various telescopes and wavelengths. The differences in beam sizes are not of great concern for this paper, since we are modeling the global SEDs here.

2.1. SCUBA images

We obtained 450 and $850 \mu\mathrm{m}$ data of II Zw 40, He 2-10 and NGC 1140, with SCUBA (Holland et al. 1999), a bolometer array on the James Clerk Maxwell Telescope (JCMT), during two observing runs during February 2000

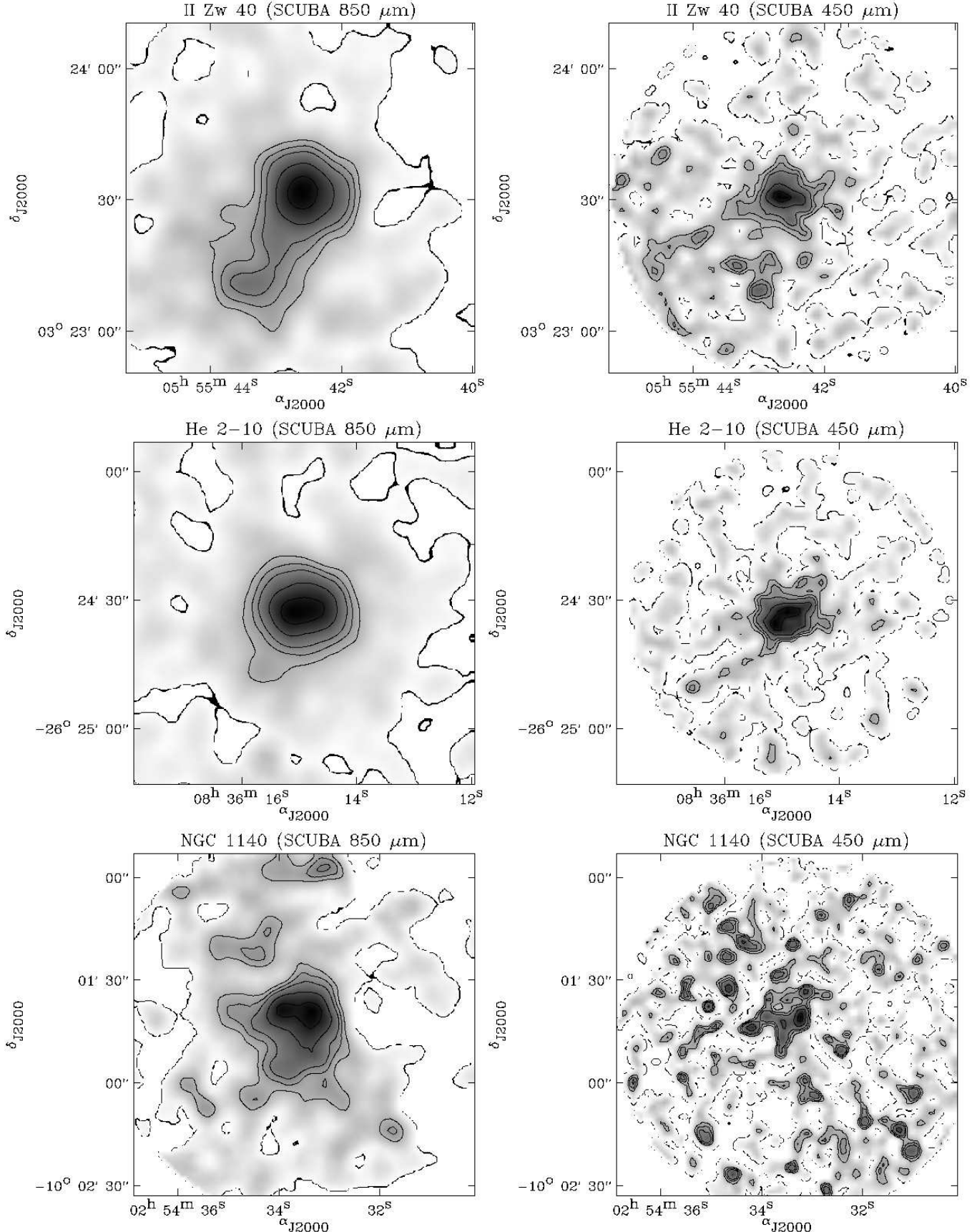


Fig. 1. SCUBA maps of the three galaxies. The first row of images is II Zw 40, the second is He 2-10, and the third is NGC 1140. The wavelength of the left column images is 850 μm and the wavelength of the right column images is 450 μm . The field of view is the same for the 450 μm and 850 μm images of each galaxy and the color table has the same dynamic range. The contours are 99, 90, 70, 50, 40 and 30 % of the peak flux values.

and December 2000. Observations were carried out in the jiggle-mapping mode using a 64-point jiggle pattern with a chop throw of $150''$. The precise data reduction method used is described in detail in paper II including details of the error analyses. The full width at half maximum (FWHM) of the beam is $8.5''$ at $450\mu\text{m}$ and $15.2''$ at $850\mu\text{m}$. The measured τ_{CSO} at 225 GHz, obtained from the Caltech Submillimeter Observatory (CSO) radiometer, ranged from 0.04 to 0.1 during our observations and our observed calibration sources were Uranus, Mars or CRL 618. The final images are shown in Fig. 1 and the fluxes are presented in Table 1. The signal-to-noise ratios of these images are: $S/N(850\mu\text{m}) \simeq 10$ and $S/N(450\mu\text{m}) \simeq 7$, for NGC 1140; $S/N(850\mu\text{m}) \simeq 15$ and $S/N(450\mu\text{m}) \simeq 11$, for II Zw 40; $S/N(850\mu\text{m}) \simeq 23$ and $S/N(450\mu\text{m}) \simeq 14$, for He 2-10.

The contamination of the $850\mu\text{m}$ fluxes, due to the CO(3-2) line, can be quantified from observations reported in the literature. Based on CSO observations, Meier et al. (2001) give an upper limit for II Zw 40 of $I_{\text{CO}(3-2)} \lesssim 0.9 \text{ K km s}^{-1}$ in $22''$, which we convert to $F_{\text{CO}(3-2)}^{850\mu\text{m}} \lesssim 3.4 \text{ mJy}$, for the total galaxy by using the deconvolved $850\mu\text{m}$ SCUBA map and assuming that the CO emission has the same spatial distribution as the cold dust. Meier et al. (2001) also give the $I_{\text{CO}(3-2)}$ for several pointings in He 2-10 which have some overlap with our SCUBA data. We took the central measurement $I_{\text{CO}(3-2)} = 16.6 \text{ K km s}^{-1}$ and scaled it in the same manner as for II Zw 40. The estimated CO(3-2) flux in the $850\mu\text{m}$ band for the total galaxy is, thus, $F_{\text{CO}(3-2)}^{850\mu\text{m}} = 30 \text{ mJy}$ (Table 1). In the case of NGC 1140, we did not find any CO(3-2) measurement, in the literature. However, this contribution should be very low considering the contribution of the CO(2-1) line in the MAMBO band (Sect. 2.2), thus we believe that this contribution is not significant.

The radio continuum contribution to our total submillimetre fluxes can be estimated by extrapolating from the numerous radio fluxes given in the literature. The radio continuum at submillimetre wavelengths is normally dominated by free-free emission in galaxies (e.g. Condon 1992). The free-free emission is described by $F_\nu \propto \nu^{-0.1}$. In the case of II Zw 40, Sramek & Weedman (1986) report a global thermal flux of $S_\nu = 13.9 - 15.2 \text{ mJy}$ at 4.8 GHz. We deduce a flux $S_\nu = 9.1 - 9.9 \text{ mJy}$ at $850\mu\text{m}$ ($\lesssim 10\%$) and $S_\nu = 8.5 - 9.3 \text{ mJy}$ at $450\mu\text{m}$ ($\lesssim 4\%$). For He 2-10, Kobulnicky & Johnson (1999) report a total flux of $F_\nu = 21.1 \pm 1.2 \text{ mJy}$ at 14.9 GHz, which we convert to $S_\nu = 14.5 - 15.4 \text{ mJy}$ at $850\mu\text{m}$ ($\lesssim 13\%$) and $S_\nu = 13.6 - 14.4 \text{ mJy}$ ($\lesssim 4\%$) at $450\mu\text{m}$. We could not find a decomposition between thermal and non-thermal flux, thus this estimate serves at the upper limit of the radio contribution in our bands. We remain conservative here in order to be sure that if we do observe a submillimetre excess arising from dust in these galaxies, as found previously in NGC 1569 (paper II), the results will not be effected by our assumptions of contamination from non-dust sources. Finally, Klein et al. (1983) report a $S_\nu = 11 \pm 3 \text{ mJy}$ flux

at 10.7 GHz, in NGC 1140. Thus, we are able to give a range of values of $S_\nu = 5.6 - 9.9 \text{ mJy}$ at $850\mu\text{m}$ ($\lesssim 12\%$) and $S_\nu = 4.9 - 8.6 \text{ mJy}$ at $450\mu\text{m}$ ($\lesssim 4\%$). These contributions are summarised in the last part of Table 1. Thus, subtracting the radio continuum and CO contributions to the observed submillimetre fluxes, we are confident that we can quantify the flux density arising from dust only.

	II Zw 40 (mJy)	He 2-10 (mJy)	NGC 1140 (mJy)
$F_{450\mu\text{m}}^{\text{tot}}$	248 ± 81	342 ± 65	272 ± 55
$F_{850\mu\text{m}}^{\text{tot}}$	98 ± 14	130 ± 12	69 ± 28
$\text{CO}(3-2)_{850\mu\text{m}}$	$\lesssim 3.4$	~ 30	-
Radio:			
- $450\mu\text{m}$	$8.5 - 9.3$	$13.6 - 14.4$	$4.9 - 8.6$
- $850\mu\text{m}$	$9.1 - 9.9$	$14.5 - 15.4$	$5.6 - 9.9$

Table 1. Flux and contributions to the submillimeter bands of II Zw 40, He 2-10 and NGC 1140. The total fluxes are not corrected for radio continuum and CO(3-2).

As noted for NGC 1569 (paper II), the morphology of the submillimetre emission (Fig. 1) is not concentrated toward the outer regions. It follows the mid-IR emission relatively well, the peak correlating with the star forming regions.

2.2. MAMBO observations

We obtained 1.3 mm data (230 GHz, bandwidth $\simeq 80 \text{ GHz}$) of II Zw 40, He 2-10 and NGC 1140, with MAMBO (Kreysa et al. 1999), a bolometer array on the IRAM 30 meter radio-telescope, during two observing runs in December 2001 and January 2002. Observations were carried out in On-Off mode using the 117-bolometer array.

The On-Off observations were conducted in standard chop-nod mode, with individual scans divided in 6 sub-scans each of which yielded 20 seconds of on+off source exposure. The secondary mirror was chopped by $55''$ in azimuth for II Zw 40 and He 2-10 and $70''$ for NGC 1140. The pointing and the focus of the telescope were checked every hour. The data were analysed with the NIC software (Broguière et al. 2002) from the GILDAS package. The data reduction included the following steps.

- 1) Atmospheric opacity: The skydip measurements were carried out every two hours. The τ_{230} , optical depth of the atmosphere at 230 GHz, varied between 0.14 and 0.35 during the observations and was below 0.2 during most of the scans. Moreover, it was relatively constant between successive skydips. Each scan was corrected for atmospheric extinction using linear interpolation of the opacity measurements obtained from the skydip preceding the scan and that following the scan.
- 2) Gain and bad bolometers: Some bolometers are known to be noisy. We flagged these currently-identified bad bolometers during the remaining procedures.
- 3) Spikes: A despiking function is applied to each bolome-

ter, with a threshold of $5 \times \sigma$. The spikes found are removed and replaced by the interpolation of the adjoining data.

4) Final signal: The mean signal of each bolometer and its variance is computed from the corresponding subscans. A baseline is removed from the raw signal by a least-square fit of a straight line to the weighted sequence of ON and OFF means. The high-frequency noise is removed from all of the channels. Finally, the flux of the reference channel is determined by removing the flux density of the adjacent four channels. If \mathcal{F}_{ib} is the flux in counts of the scan i in the bolometer b , we calculate the mean, $\mathcal{F}_b = \langle \mathcal{F}_{ib} \rangle_{\text{scans}}$, of every scan flux, \mathcal{F}_{ib} , weighted by $1/\sigma_i^2$, where $\sigma_i = \sigma(\mathcal{F}_{ib})_{\text{bolo}}$ is the deviation of each scan. We subtract the foreground emission which is determined from the mean flux of the bolometers which are not on the source. Thus, the final signal of each bolometer is $\mathcal{F}_b^{\text{corr}} = \mathcal{F}_b - \langle \mathcal{F}_b \rangle_{b - \{\text{source}\}}$. These $\mathcal{F}_b^{\text{corr}}$ are plotted in Fig. 2 for the two galaxies which are detected.

5) Calibration: Mars, α Ori, NGC 7538 and $\text{HL}\tau$ were observed daily as primary and secondary calibrators. The calibration data were reduced in the same way as other galaxies. We compute a flux conversion factor, Φ , which provides the relationship between counts and astrophysical fluxes (in Jy), averaged over the calibrators. The flux of our sources is converted to astrophysical flux values (in Jy/beam), $F_b = \Phi \times \mathcal{F}_b^{\text{corr}}$, by multiplying the signal by the conversion factor. We use the submillimeter spatial distribution to scale this flux to the total flux of each galaxies. First, we deconvolve the SCUBA 850 μm maps with a multi-resolution Lucy algorithm from the MR/1 package (Starck et al. 1998), using a 3σ detection threshold. Second, we convolve this image to the IRAM 30-meter beam and we extract the ratio of the total flux to the flux in one beam, $\mathcal{R} = F_{\nu}^{\text{tot}}(850\mu\text{m})/F_{\text{beam(IRAM)}}(850\mu\text{m})$. We multiply the IRAM flux in Jy/beam by this ratio to obtain the total flux at 1.3 mm, $F_{\nu}^{\text{tot}}(1.3\text{ mm}) = F_{b_{\text{ref}}} \times \mathcal{R}$, where b_{ref} is the reference bolometer. The final fluxes are given in Table 2; the values of \mathcal{R} is given in the last part of this table.

6) Error estimation: The error on the total flux is given by $\Delta F_{\nu}^{\text{tot}}(1.3\text{ mm}) = \Delta F_{b_{\text{ref}}} \mathcal{R} + F_{b_{\text{ref}}} \Delta \mathcal{R}$. The error on the aperture, $\Delta \mathcal{R}$, is estimated by shifting the SCUBA image convolved by the IRAM beam by $\pm 3''$ in RA and DEC. This $3''$ error is the typical IRAM pointing error (Wild 1999) and is consistent with deviations observed during the pointing verification measurements during the observations. The error on the flux in one beam, $\Delta F_{b_{\text{ref}}}$, is the quadratic sum of two components: $(\Delta F_{b_{\text{ref}}})^2 = \sigma^2(F_{b - \{\text{source}\}}) + (\Delta \Phi/\Phi)^2$. The first component, $\sigma(F_{b - \{\text{source}\}})$, is the RMS of the final signal. The second component, $\Delta \Phi/\Phi$, is the relative deviation of the flux conversion factor over the various calibrators. The various contributions to the error are given in percentage in Table 2.

7) Non-dust contamination: The expected contamination from the CO(2-1) line can be quantified from measurements in the literature. In the case of II Zw 40, we estimate 0.1 mJy due to the CO(2-1) line in the IRAM 1.3 mm

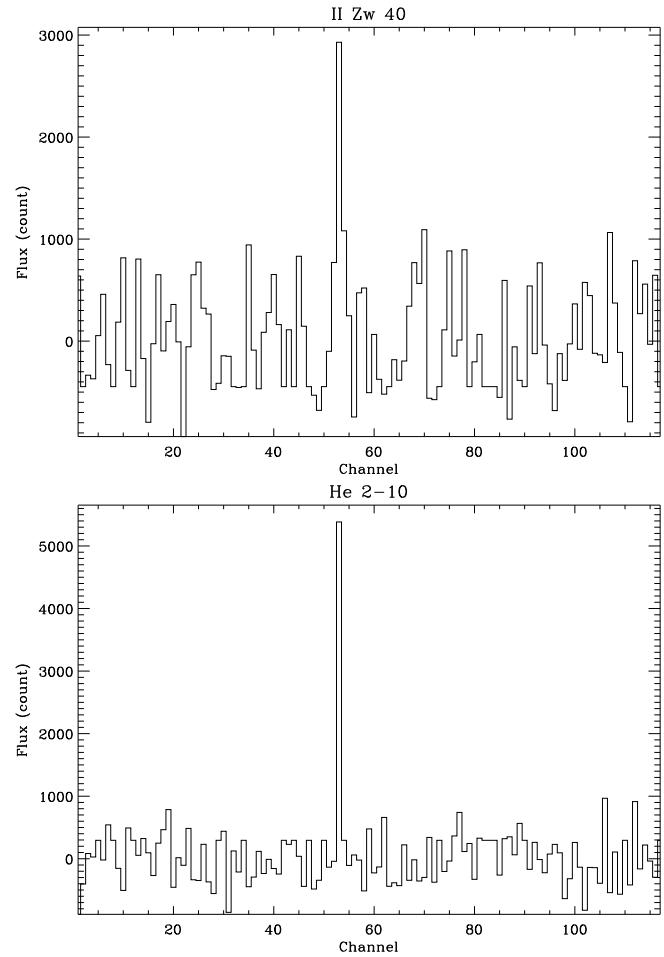


Fig. 2. On-Off observations for the two detected galaxies, II Zw 40 and He 2-10. These plots show the signal in each bolometer after foreground subtraction. The peak corresponds to the reference channel (n° 53) which is centered on the source. The other channels are assumed to see the sky.

broadband from Sage et al. (1992). For He 2-10, we estimate a flux of 4 mJy in a $12.5''$ aperture from Baas et al. (1994), and scale it to ~ 5 mJy for the total galaxy. The upper limit given by Hunter & Sage (1993), for NGC 1140, gives a CO(2-1) flux in the IRAM band of $\lesssim 0.02$ mJy. The radio continuum component can be extrapolated from radio fluxes that we used in Sect. 2.1. In the case of II Zw 40, we deduce a flux $S_{\nu} \simeq 9.5 - 10.3$ mJy at 230 GHz ($\lesssim 24\%$); for He 2-10, $S_{\nu} \lesssim 15.1 - 17.0$ mJy at 230 GHz ($\lesssim 28\%$) and $S_{\nu} \simeq 5.9 - 10.3$ mJy at 230 GHz for NGC 1140 ($\simeq 20\%$). These contributions are summarised in Table 2.

2.3. Infrared data

The details and the data treatment of the ISOCAM CVF mid-IR observations are presented in paper I. We found that the slope of the mid-IR spectrum is a critical factor in constraining the dust model, particularly in the 5 to 16 μm wavelength range (paper II). Thus, using only the

	II Zw 40	He 2-10	NGC 1140
	(mJy)	(mJy)	(mJy)
$F_{\nu}^{\text{tot}}(1.3 \text{ mm})$	43 ± 13	60 ± 14	$\lesssim 48$
Radio cont.	$9.5 - 10.3$	$15.1 - 17.0$	$5.9 - 10.3$
CO(2-1) line	0.1	4	$\lesssim 0.02$
RMS error	17 %	2 %	100 %
$\Delta\Phi/\Phi$	16 %	12 %	16 %
$\Delta\mathcal{R}$	22 %	25 %	30 %
$1/\mathcal{R}$	41 %	48 %	22 %

Table 2. Contributions to the 1.3 millimeter fluxes of II Zw 40, He 2-10 and NGC 1140. The total fluxes, $F_{\nu}^{\text{tot}}(1.3 \text{ mm})$, are not corrected for radio continuum and CO(2-1).

IRAS 12 μm band does not provide sufficient constraints on the mid-IR SED which predominantly traces the hot dust component. From a fit of the spectrum in II Zw 40, we find that the internal extinction is $A_V \simeq 15$ (paper I). We use the dereddened spectrum in the modeling. We characterised the mid-IR dust continuum by choosing a few wavelength regions of the CVF which do not contain aromatic bands or ionic lines (Table 4).

IRAS fluxes for II Zw 40 and NGC 1140 are given by Hunter et al. (1989) and by Melisse & Israel (1994). Thronson & Telesco (1986) also give the IRAS fluxes for II Zw 40. The values for the four IRAS broadbands given by these authors are consistent. Moreover, the 12 μm IRAS flux is consistent with the ISOCAM CVF spectrum integrated into this band (paper I). For our modeling purposes, we use the values of Hunter et al. (1989) since error bars are also provided. These fluxes have been color-corrected. We use the IRAS fluxes for He 2-10 from Sauvage et al. (1997).

In the case of II Zw 40, an additional 20 μm flux of $1.0 \pm 0.2 \text{ Jy}$ is given by Roche et al. (1991). For He 2-10, we consider the flux at 11.65 μm reported by Sauvage et al. (1997), who also give a N band flux for He 2-10. However we use the N band flux from Vacca et al. (2002) instead, since there is a large discrepancy between this flux and that cited by Sauvage et al. (1997) (see the discussion by Vacca et al. 2002). We include an unpublished M band observation of He 2-10 (Sauvage & Vanzi 2005) in our SED.

2.4. Optical data

To constrain the input stellar radiation field we use optical data from the literature. There are several papers reporting optical observations of II Zw 40, He 2-10 and NGC 1140. We choose magnitudes explicitly given for the total galaxy and where the authors specified the Galactic foreground extinction corrections. Preference was given to measurements quantifying the uncertainties. In some cases, we were obliged to scale data which were given for an aperture smaller than the total size of the galaxy.

In the case of II Zw 40, we used B, V, R and I magnitudes from Cairós et al. (2001) and U magnitude from

the RC3 catalog (de Vaucouleurs et al. 1991). The B magnitude, given by Cairós et al. (2001) is also consistent with that provided by Heisler & Vader (1994), Deeg et al. (1997) and de Vaucouleurs et al. (1991). The V magnitude of Cairós et al. (2001) is consistent with that of de Vaucouleurs et al. (1991) and the R and I magnitudes are consistent with Deeg et al. (1997). The J, H and K fluxes of II Zw 40 reported by Vanzi et al. (1996) for an aperture of 27'', were scaled to obtain values for the entire galaxy. We computed the scaling factors from the original images (Vanzi et al. 1996).

He 2-10 has been observed by Johansson (1987) in U, B, V, R, I, J, H and K bands in several apertures. U, B and V observations are given for the total galaxy (aperture of 61''), while the other bands have been observed in, at most, a 31'' aperture. The difference is relatively small (15 %). We scaled the 31'' flux measurements to fit the U, B, V bands in the total galaxy aperture. The error bars were not provided by the author. Consequently, we took the deviation of the two sets of observations reported by the author and added the error induced by the differences of apertures. Even with these considerations, the uncertainties we obtained are relatively small and may be underestimated.

For NGC 1140, we used U, B, V, R and I magnitudes from Gallagher & Hunter (1987) and J, H and K magnitudes from Hunter & Gallagher (1985). Buat et al. (2002) also observed NGC 1140 around 0.1 μm , in a $30'' \times 30''$ aperture which we believe encompasses the majority of the emission of the galaxy at these wavelengths, which is concentrated within a diameter $< 3 \text{ kpc}$ (Hunter et al. 1994b).

These data, summarised in Table 3, are used to constrain the stellar SED.

Band (μm)	II Zw 40	He 2-10	NGC 1140
	Flux (mJy)	Flux (mJy)	Flux (mJy)
0.36 (U)	15.3 ± 2.3	63.2 ± 2.1	15.1 ± 2.3
0.44 (B)	23.8 ± 1.6	90.8 ± 3.0	21.2 ± 3.2
0.55 (V)	32.9 ± 6.3	100.7 ± 5.0	23.6 ± 3.5
0.64 (R)	36 ± 11	122.1 ± 4.0	26.8 ± 4.0
0.79 (I)	29.3 ± 9.7	126.5 ± 4.1	35.2 ± 5.3
1.26 (J)	20.6 ± 4.1	147.9 ± 4.8	36.4 ± 5.5
1.60 (H)	21.9 ± 3.3	175.4 ± 5.7	40.1 ± 6.0
2.22 (K)	18.5 ± 2.8	130.2 ± 7.5	28.6 ± 4.3

Table 3. Optical data from the literature (references in the text). These fluxes are global values, corrected for the foreground Galactic extinction but not for internal extinction.

3. Self-consistent modeling of the global SED

The modeling of the global SEDs of II Zw 40, He 2-10 and NGC 1140 is done using the exact same procedure as described in paper II, for the case of NGC 1569. We refer to

this paper for the detailed description of the procedure we use here. The main steps are the following.

- UV-to-optical data from the literature (Table 3), corrected for the Galactic extinction are used to constrain the stellar radiation field. This radiation field is modeled with PÉGASE (Fioc & Rocca-Volmerange 1997), a stellar evolutionary synthesis model. We consider two instantaneous bursts of star formation representing the young stellar population created by the recent starburst and the old underlying population. We are only interested in the shape of the ISRF here, and the age is a free parameter. Hence, the initial metallicity is not of great concern, due to the age-metallicity degeneracy (e.g. Le Borgne et al. 2004). However, for a given metallicity, several age combinations fit the observations.
- The stellar population age degeneracy is removed by constraining a photoionisation model (CLOUDY; Ferland 1996) with the mid-IR ionic line ratios that we measure (paper I).
- This radiation field is used to heat the dust which is modeled with the Désert et al. (1990, hereafter DBP90) model. We fit the observed IR SED by varying the dust size distribution. The solution allows us to synthesize an extinction curve self-consistent with the emission properties.
- We iterate this process, correcting the UV-to-optical data for internal extinction with the synthesized extinction curve, until we reach an agreement between the extinction and emission. Only the spectral dependency of the extinction curve is taken into account. The global internal optical depth is deduced from the energy balance between stars and dust:

$$F_{\star} = F_{\text{UV-opt}} + F_{\text{IR-mm}}, \quad (1)$$

where F_{\star} is the intrinsic flux emitted by the stars, $F_{\text{UV-opt}}$, the escaping stellar flux, and $F_{\text{IR-mm}}$, the flux reemitted by the dust (these fluxes are integrated over frequency).

3.1. The observed SEDs

The stellar SEDs are constrained by the fluxes in Table 3 and by mid-IR ionic line ratios (paper I). The [Ne II] (12.81 μm) line is not detected in II Zw 40, thus, in this case, we constrain the photoionisation model with only two ratios: [S IV]/[Ne III] and [Ar III]/[Ne III]. In the case of He 2-10, we do not have an ISO-CAM CVF spectrum. However Beck et al. (1997) report NASA IRTF mid-IR spectroscopy of this galaxy and they measure ionic line intensities. We deduce from this study, the ratios [Ne II]/[Ar III] = 12.5 \pm 5.2 and [Ne II]/[S IV] = 50 \pm 40.

The dust SEDs are constrained by the data points shown in Table 4. All the non-dust contributions have already been subtracted from these fluxes listed in Table 4.

3.2. The dust model

As in paper II, we define an effective radius of the galaxies, R_{eff} , which is the effective distance between stars and dust in a thin shell model. We estimate the equivalent radius, R_{equiv} , by fitting an ellipse to the 850 μm images and $R_{\text{eff}} = 3/4 \times R_{\text{equiv}}$.

For II Zw 40, we assume a distance of $D = 10 \pm 1$ Mpc and for He 2-10, we assume $D = 9 \pm 1$ Mpc, consistent with all the recent values adopted in the literature (Roche et al. 1991; Conti 1991; Vacca & Conti 1992; Telesco et al. 1993). In the case of NGC 1140, we adopt $D = 23 \pm 2$ Mpc to be consistent with the recent values of 20 to 25 Mpc (Kinney et al. 1993; Hunter et al. 1994a; Saikia et al. 1994; Heckman et al. 1998; Buat et al. 2002). The relevant model parameters for the sources are given in Table 5.

Name	R_{eff} (kpc)	D (Mpc)	$M(\text{H I})$ (M_{\odot})	Z/Z_{\odot}
II Zw 40	0.5 ± 0.2	10 ± 1	4.4×10^8 ^a	$\sim 1/6$ ^b
He 2-10	0.8 ± 0.3	9 ± 1	3.1×10^8 ^c	$\sim 1/1$ ^d
NGC 1140	2.6 ± 0.9	23 ± 2	7.5×10^9 ^e	$\sim 1/3$ ^f

Table 5. Physical parameters of II Zw 40, He 2-10 and NGC 1140. R_{eff} is deduced from our mid-IR and submillimetre images, the other parameters are found in the literature. D is the distance to the galaxy and Z , the metal abundances. (a) van Zee et al. (1998); (b) e.g. Walsh & Roy (1993), Masegosa et al. (1994); (c) Sauvage et al. (1997); (d) Kobulnicky et al. (1999); (e) Hunter et al. (1994a); (f) Guseva et al. (2000).

The DBP90 dust model was originally designed to explain the dust properties of the Milky Way and includes three dust components: the Polycyclic Aromatic Hydrocarbons (PAHs) which are responsible for the mid-IR emission features at 3.3, 6.2, 7.7, 8.6 and 11.3 μm , the Very Small Grains (VSGs), which are assumed to be the carriers of the 2175 \AA extinction bump and the Big Grains (BGs), which have an emission peak in the far-IR. VSGs are carbonaceous grains and BGs are silicate grains. Each of the 3 dust components is described by their minimum and maximum grain size (a_- and a_+), and α , the index of the power law size distribution which is $n(a) \propto a^{-\alpha}$ (a is the grain radius and $n(a)$ is the number density of grains between a and $a + da$). The dust mass abundance of each component is $Y = M_X/M_H$, where M_X is the mass of the dust component, X , and M_H is the hydrogen mass in the galaxy.

4. Results and discussion

4.1. The model parameters

We attempt to fit the observed SED with the DBP90 dust model, varying the dust parameters for each component. We retain the original denomination of BGs, even if the

Instrument	II Zw 40		He 2-10		NGC 1140	
	λ (μm)	Flux (mJy)	λ (μm)	Flux (mJy)	λ (μm)	Flux (mJy)
ISOCAM	8.8	89 ± 55			6.1	41 ± 26
	9.4	132 ± 47			6.2	89 ± 22
	10.1	177 ± 64			6.5	46 ± 25
	10.8	238 ± 64			6.9	55 ± 21
	11.8	315 ± 65			7.4	82 ± 21
	12.1	339 ± 67			7.6	119 ± 20
	13.2	417 ± 73			7.8	113 ± 20
	13.9	458 ± 75			7.9	120 ± 21
	14.6	489 ± 69			8.1	65 ± 20
	15.0	504 ± 78			10.9	82 ± 15
	16.0	532 ± 87			11.1	149 ± 17
					11.3	192 ± 17
					11.5	118 ± 18
					11.7	90 ± 16
					13.4	91 ± 23
					13.9	62 ± 20
					14.4	89 ± 23
					16.1	78 ± 35
Others	20 (Q)	1000 ± 200	4.8 (M) 10.1 (N) 11.65	60 ± 9 720 ± 95 850 ± 100		
IRAS			12	1100 ± 160		
	25	2170 ± 300	25	6550 ± 980	25	390 ± 70
	60	7280 ± 900	60	23800 ± 3600	60	3940 ± 600
	100	6360 ± 1100	100	31800 ± 4800	100	5000 ± 800
SCUBA	443	241 ± 81	443	328 ± 67	443	270 ± 110
	863	87 ± 14	863	85 ± 36	863	69 ± 28
MAMBO	1200	33 ± 13	1200	40 ± 18	1200	$\lesssim 42$

Table 4. Observed dust SED. The data are the flux values used to constrain the dust model. They are corrected for all non-dust effects (molecular lines, radio continuum) and extinction. The references are given in the text in Sect. 2. For NGC 1140, the ISOCAM data which are reported are those used to constrain both the continuum and the PAH bands. The VSGs have been constrained separately (see explanation in text).

model results indicate that these grains are small, as in the cases reported here. The values of the parameters of the best χ^2 fits to the SEDs (Fig. 3) are given in Table 6.

The bulk of the emission originates essentially in the VSGs and BGs (Fig. 3). The free parameters are a_+ , α and Y , for the VSGs, and a_- , α and Y , for the BGs. We fix a_+^{BG} to the Galactic value, since its determination from the fit is very uncertain, the large sizes not being significant contributors to the emission. For He 2-10 and NGC 1140, we also fix a_-^{VSG} to the Galactic value, since the best χ^2 is obtained for very low unphysical values (a few Å). On the other hand, for II Zw 40, the value of a_- can be determined. Among our sources, He 2-10 is the most poorly constrained, we do not have a CVF spectrum. However the number of free parameters remains smaller than the number of observations (Table 6). Since the PAH emission is detected only in NGC 1140, Y_{PAH} remains a free parameter. For II Zw 40 and He 2-10, we are able to put only an upper limit on the PAH mass.

Our results show that the three component DBP90 dust model is not adequate to explain the full dust SED out to millimetre wavelengths for any of the galaxies, as we first discovered in NGC 1569 (see paper II for this point).

We are compelled to add a fourth component for each of the galaxies. The Very Cold Grains (VCGs) are modeled using a modified black body, with emissivity indices of $\beta = 1$ (consistent with carbonaceous grain properties) and $\beta = 2$ (consistent with silicate grain properties). This very cold dust component is constrained, only by the three submillimetre observations. Thus it is very difficult to constrain the temperature, the mass and the β of this component. We choose to vary only the temperature T and the mass of this component, considering the different values of β . However, for II Zw 40 and He 2-10, the fit with $\beta = 2$ gives a dust mass higher than the metal mass of the galaxy, thus we exclude this value and fit only a $\beta = 1$ black body. In the case of NGC 1140, we only have an upper limit on the flux at 1.3 mm, so we do not have sufficient data to constrain the value of β .

Table 6 contains the values of several statistical quantities: n is the number of observations, m , the number of free parameters used for the standard model, m_{VCG} , the number of free parameters after the introduction of the VCGs, $\bar{\chi}^2 = \chi^2/(n - m - 1)$ is the reduced chi square, for the standard model, and $\bar{\chi}^2_{\text{VCG}}$, the reduced chi square with VCGs.

		Milky Way	NGC 1569	II Zw 40	He 2-10	NGC 1140
PAHs	Y	4.3×10^{-4}	$\lesssim 1 \times 10^{-6}$	$\lesssim 5 \times 10^{-7}$	$\lesssim 3 \times 10^{-6}$	8.3×10^{-7}
	a_-	0.4 nm	0.4 nm	0.4 nm	0.4 nm	0.4 nm
	a_+	1.2 nm	1.2 nm	1.2 nm	1.2 nm	1.2 nm
	α	3.0	3.0	3.0	3.0	3.0
VSGs	Y	4.7×10^{-4}	1.8×10^{-5}	2.3×10^{-5}	4.9×10^{-5}	2.2×10^{-5}
	a_-	1.2 nm	1.2 nm	2.0 nm	1.2 nm	1.2 nm
	a_+	15 nm	7.8 nm	2.9 nm	2.6 nm	3.0 nm
	α	2.6	4.0	1.0	5.5	7.9
BGs	Y	6.4×10^{-3}	4.4×10^{-4}	2.6×10^{-4}	8.9×10^{-4}	6.1×10^{-4}
	a_-	15 nm	2.2 nm	3.2 nm	2.5 nm	3.8 nm
	a_+	110 nm	110 nm	110 nm	110 nm	110 nm
	α	2.9	6.3	25	8.9	30
VCGs	Y	unknown	1.3×10^{-3}	1.3×10^{-3}	1.5×10^{-3}	$\sim 1.1 \times 10^{-3}$
	T	unknown	5 K	8 K	6 K	~ 5 K
	β	unknown	1	1	1	~ 1
Statistics	n	-	18	18	10	24
	m	-	7	7	6	7
	m_{VCG}	-	9	9	8	10
	χ^2	-	1.7	4.5	9.8	1.5
	χ^2_{VCG}	-	0.27	0.36	2.8	0.89
	ΔAIC	-	46	67	25	52
	$\Delta AICC$	-	61	82	149	58

Table 6. Dust parameter values and statistical quantities, for the best model fit. For comparison, we give the corresponding values for the Milky Way (DBP90) and for NGC 1569 (paper II).

The introduction of the VCGs, having important astrophysical consequences, should be examined with scrutiny. Hence, we have calculated the Akaike's Information Criterion (AIC), in order to examine the validity of introducing this new component. The AIC is a statistical quantity that can be regarded as the extension of the log likelihood, including the effect of the instability induced by the number of parameters. An elementary derivation of the AIC can be found in Takeuchi (2000), and a brief summary of its use in Appendix of Takeuchi et al. (2000). The squared sum of the deviations of the model from the data is:

$$S = \sum_{i=1}^n [\log(L_{\nu i}) - \log(f(\lambda_i, \theta))]^2, \quad (2)$$

$L_{\nu i}$ being the observed monochromatic luminosity at the wavelength λ_i , $f(\lambda_i, \theta)$, the value of the model at the same wavelength, and θ , the parameter vector. The AIC is defined by:

$$AIC = n \times \ln(2\pi + 1) + n \times \ln\left(\frac{S}{n}\right) + 2(m + 1). \quad (3)$$

The second order corrected AICC is:

$$AICC = AIC + \frac{2(m + 1)(m + 2)}{n - m - 2}. \quad (4)$$

A variation of AIC and AICC greater than unity, after introducing the VCGs, is required to justify this new component. Table 6 contains the values of $\Delta AIC = AIC_{\text{standard}} - AIC_{\text{VCG}}$ and $\Delta AICC$ which is defined identically. We see that these variations are much larger than unity, thus the VCG component is statistically reasonable.

The range of reliability of the parameters is provided in Table 7. The uncertainties of the parameters in Table 7 are derived from both the uncertainty of the geometry (the value of R_{eff}) and the errors of the observations (Section 2). A complete description of the way we compute these errors is given in paper II (Sect. 4.1.2).

4.2. The size distributions

The size distributions are shown in Fig. 4. Compared to the Galaxy, there is an obvious dearth of PAHs and the mass spectrum is dominated by grains of small sizes (radius $a \simeq 3 - 4$ nm) as shown in Fig. 4. The power-law size distributions for all of the galaxies are qualitatively similar. The preference for grains of small sizes may be due to the high supernovae rate in these galaxies. Supernovae produce shocks that fragment and erode the large grains and produce smaller grains (Jones et al. 1996), as we demonstrate in paper II where we use the shock model of Jones et al. (1996) to explain the shape of the size distribution of NGC 1569. The effect is similar here for II Zw 40, He 2-10 and NGC 1140.

4.3. The modeled SEDs

4.3.1. The ISRFs

Fig. 5 shows the synthesized radiation fields for our galaxy sample and we compare these with that of the Galaxy in Fig. 6. In the dwarf galaxies with evidence for current starburst activity, the effective, global radiation field as seen by the dust, is more intense and harder than that

		NGC 1569	II Zw 40	He 2-10	NGC 1140
PAHs	Y	$\sim 0 - 10^{-6}$	$\sim 0 - 5 \times 10^{-7}$	$\sim 0 - 3 \times 10^{-6}$	$(0.5 - 1.4) \times 10^{-6}$
VSGs	Y	$(1.3 - 2.3) \times 10^{-5}$	$(1.4 - 3.8) \times 10^{-5}$	$(2.8 - 7.5) \times 10^{-5}$	$(1.1 - 2.8) \times 10^{-5}$
	a_-	1.2 nm <i>fixed</i>	1.1 – 2.5 nm	1.2 nm <i>fixed</i>	1.2 nm <i>fixed</i>
	a_+	3.5 – 12 nm	2.1 – 5.0 nm	1.9 – 2.7 nm	2.0 – 3.0 nm
	α	2.6 – 5.2	0.2 – 3.7	2.8 – 7.1	3.2 – 36
BGs	Y	$(3.5 - 4.7) \times 10^{-4}$	$(1.9 - 4.0) \times 10^{-4}$	$(0.5 - 1.5) \times 10^{-3}$	$(0.3 - 1.1) \times 10^{-3}$
	a_-	2.1 – 2.9 nm	3.0 – 3.7 nm	1.7 – 2.6 nm	3.7 – 4.0 nm
	a_+	110 nm <i>fixed</i>	110 nm <i>fixed</i>	110 nm <i>fixed</i>	110 nm <i>fixed</i>
	α	5.8 – 35	25 – 37	4.8 – 15.5	23 – 40
VCGs	Y	$(1.3 - 0.4) \times 10^{-3}$	$(2.0 - 0.7) \times 10^{-3}$	$(0.7 - 4.1) \times 10^{-3}$	$(1.7 - 0.2) \times 10^{-3}$
	T	5 – 7 K	7 – 9 K	5 – 7 K	5 – 9 K
	β	1 <i>fixed</i>	1 <i>fixed</i>	1 <i>fixed</i>	1 – 2

Table 7. Range of reliability of the dust parameters. For comparison, we give the corresponding values for NGC 1569 (paper II). These limits take into account both the spread due to the error bars of the observations and the spread due to the assumed value of the radius. The indices of the power-law distribution, α , have high uncertainties since the size distribution is very steep. For these cases, the choice of a single grain size would effectively fit the emission. “Fixed” indicates that these parameters are fixed to the Galactic values due to the lack of constraints.

of the Galaxy. In paper I we discussed the correlation between the hardness and intensity of the ISRF and the lack of PAHs in the starbursting dwarf galaxies, while, PAHs are observed to be abundant throughout the Galaxy. We see an evolutionary sequence among these four galaxies. NGC 1140, where PAHs are evident, is the most quiescent galaxy of the sample, with a radiation field that is less intense and relatively soft compared to the other galaxies (Fig. 6; paper I). In the three other dwarf galaxies, NGC 1569, II Zw 40 and He 2-10, PAH bands are very weak, if present at all (paper I). Likewise, the ISRFs are intense and hard. Among these three starbursting dwarf galaxies, NGC 1569 has a softer ISRF and the aromatic bands seen in the CVF spectrum are present, even if very weak, contrary to II Zw 40, where there is no evidence for the PAH band emission in the CVF spectrum.

4.3.2. The dust emission

The best χ^2 modeled dust SEDs, after iteration, are plotted in Fig. 3 and compared to that of the Galaxy in Fig. 7. The characteristics of the 3 newly-presented dust SEDs have many similarities to those already deduced for NGC 1569, in paper II.

The SEDs indicate overall hotter dust, peaking at $\sim 60 \mu\text{m}$. Due to the small grain size distributions of the PAH, VSG and BG components, most of the grains are stochastically heated and are not in thermal equilibrium with the radiation field in these galaxies. Table 8 contains the temperature range of each component for the maximum and minimum sizes compared to Galactic values. In paper II, we estimated the transition grain radius, a_t , between stochastic heating and thermal equilibrium to have an idea over what range of dust sizes it is important to consider the process of stochastic heating. This is a function of the radiation field, the dust size and the heat capacity of the dust. We refer to Section 4.1.3 of paper II for a detailed explanation of the calculation. In Fig. 8, we

compare the variation of the cooling rates and the photon absorption rates as a function of the radius, for a single BG. The point where the two curves intersect gives an idea of the grain radius, a_t , below which the stochastic heating becomes dominant. These transition radii are $a_t \simeq 5 \text{ nm}$ in NGC 1569, $a_t \simeq 4 \text{ nm}$ in II Zw 40 and He 2-10, $a_t \simeq 6 \text{ nm}$ in NGC 1140 and $a_t \simeq 9 \text{ nm}$ in the Galaxy. These estimates demonstrate that the grains become stochastically heated at smaller radii, due to the higher intensity of the radiation field (Fig. 6). By comparing the estimates of a_t with the typical radius that dominates the mass spectrum of the grains, which is $a \simeq 3 - 4 \text{ nm}$ (Fig. 4), we deduce that most of the grains are stochastically heated in these galaxies. Even at wavelengths as long as $60 \mu\text{m}$, where the dust emission peaks, the grains are primarily stochastically heated.

Another striking feature of the dust emission spectra is the weakness or absence of the mid-IR PAH emission bands particularly in NGC 1569 and II Zw 40 (the mid-IR spectra are presented in paper I). He 2-10 has not been observed with the ISOCAM CVF. However, Martín-Hernández et al. (2005, *private communication* from Marc Sauvage) have obtained a ground-based mid-IR spectrum in the range $8 - 13 \mu\text{m}$ which also reveals a lack of PAH features. Therefore, for these three galaxies, we only put an upper limit on the PAH mass, given by the continuum emission of this component. We do not actually fit the bands in the model. In the case of NGC 1140, we see relatively significant PAH emission, allowing us to properly constrain the PAH mass. For this purpose, we use a modified version of the DBP90 model (Laurent Verstraete, *private communication*) where the PAH emission features are modeled more precisely (Fig. 3). The optical constants are deduced from a spectrum of a typical H II region. For NGC 1140, we use the process of decomposition of the ISOCAM mid-IR spectrum described in paper I: the PAH features are modeled as Lorentzian bands; the ionic lines are modeled as

		NGC 1569		II Zw 40		He 2-10		NGC 1140		Galaxy	
		T_{\min}	T_{\max}								
PAH	a_-	2.7 K	9200 K	2.7 K	4400 K						
	a_+	2.7 K	1800 K	2.7 K	1100 K						
VSG	a_-	2.7 K	890 K	2.7 K	490 K	2.7 K	890 K	2.7 K	890 K	2.7 K	630 K
	a_+	2.7 K	160 K	2.7 K	350 K	2.7 K	380 K	2.7 K	340 K	2.7 K	78 K
BG	a_-	2.7 K	230 K	2.7 K	140 K	2.7 K	190 K	2.7 K	111 K	15 K	22 K
	a_+	28 K	28 K	30 K	30 K	31 K	31 K	20 K	20 K	17 K	17 K

Table 8. Temperatures of the PAH, VSG and BG components for NGC 1569 (paper II), II Zw 40, He 2-10 and NGC 1140 compared to those of the Galaxy (DBP90). We give the minimum (T_{\min}) and maximum (T_{\max}) temperatures for each component. All the grains, except the largest BGs (for which $T_{\min} = T_{\max} = T_{\text{equilibrium}}$), are stochastically heated. The values of T_{\max} given for the PAHs are larger than the vaporisation temperature, thus they are unphysical. The minimum temperature never reaches values below T_{CMB} , since all grain sizes are in equilibrium with the very low energy input coming from the CMB.

Gaussian emission lines and the continuum is fitted as a modified black body providing a constraint on the VSG component in the dust model. Then, we add the PAH part of the model to fit the entire spectrum, including the aromatic bands.

For each SED of our sample, we are left with a submillimetre/millimetre excess that we cannot explain with the standard DBP90 model. As originally found for NGC 1569, we are compelled to invoke the presence of an ubiquitous very cold grain component (VCGs) in II Zw 40, He 2-10 and NGC 1140. Various hypotheses for this excess are fully explored in paper II. They include: very cold dust, change of grain optical properties at long wavelengths and grain-grain coagulation. We modeled the VCG component using a modified black body (Sect. 4.1). The temperatures of these VCG components are $T = 5 - 9$ K (Table 7). We have shown in paper II (Sect. 4.5) that the VCG component could correspond to very cold dust embedded in very dense clumps. Other means to increase the submillimetre emissivity which we see in these galaxies could be different optical properties due to temperature effects, as well as grain-grain coagulation. The temperature dependent optical properties are considered in paper II and in the Appendix B of the present paper, but so far failed to produce better fits. Thus, in paper II, as well as the present paper, we chose to discuss the very cold dust hypothesis, since it has a number of quantifiable consequences (Sect. 4.6).

4.4. The extinction curves

From the dust properties described by the parameters in Tables 6 and 7, we synthesize an extinction curve assuming a simple screen attenuation of the radiation. Construction of the extinction curve is based on the DBP90 model assumptions of the PAHs being the carriers of the FUV non-linear rise; the carbonaceous VSGs giving rise to the 2175 Å extinction bump (e.g. Savage & Mathis 1979) and the BGs giving rise to the NIR and visible rise of the extinction curve. The individual contributions to the extinction curves and the total synthesized extinc-

tion curves are displayed in Fig. 9 and are compared to the Milky Way (DBP90), the Large Magellanic Cloud (Koornneef & Code 1981; Nandy et al. 1981) and one line of sight toward the Small Magellanic Cloud (Prévot et al. 1984) in Fig. 10.

These synthesized global extinction curves are characterised by a quasi-linearity with $1/\lambda$ which is also the case for the extinction curves seen toward the Magellanic Clouds (Fig. 10). These slopes indicate a higher absorption in the UV as a consequence of the presence of the small sizes of the BGs, as can be seen on the decompositions in Fig. 4, and also due to the lack of PAHs which are responsible for the far-UV rise. We also note that the 2175 Å extinction bump is lower in NGC 1569, He 2-10 and NGC 1140 than in the Milky Way, as is the case for the extinction curves observed toward a line of sight in the low-metallicity Magellanic Clouds. This is a consequence of the higher silicate-over-graphite ratio ($M_{\text{BG}}/M_{\text{VSG}}$), in these galaxies than in the Milky Way (this ratio is equal to 14 for the Milky Way, and to 24, 18 and 28 for NGC 1569, He 2-10 and NGC 1140, respectively, from Table 6). Indeed, in the DBP90 model, the carriers of the bump are the VSGs. However, the ratio $M_{\text{BG}}/M_{\text{VSG}}$ is smaller in II Zw 40 ($M_{\text{BG}}/M_{\text{VSG}} \simeq 11$), which explains why the model determines a larger bump in II Zw 40. The silicate-graphite ratio is not constrained very accurately as can be seen from the error bars on our parameters in Table 7. Moreover, the carriers of the bump could be other species of grains like the PAHs, as proposed by Joblin et al. (1992). In recent dust models (Draine & Li 2001; Li & Draine 2001; Zubko et al. 2004), the carriers of the bump are both PAHs and solid carbonaceous grains. Thus, the lack of PAHs could naturally explain the weakness of the bump in these galaxies.

We think, as already suggested e.g. by Mas-Hesse & Kunth (1999) and Weingartner & Draine (2001), that the shape of the extinction curve, thus the very different dust properties, essentially reflects the starburst activity in these galaxies, rather than a consequence of their low metallicity. Indeed, the fragmentation and the erosion of the grains by the numerous shock

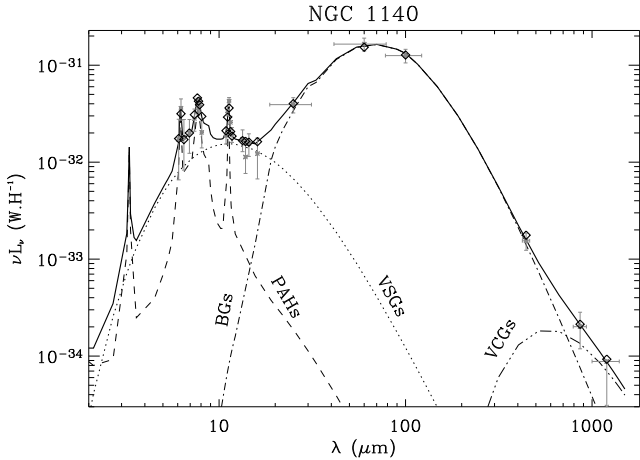
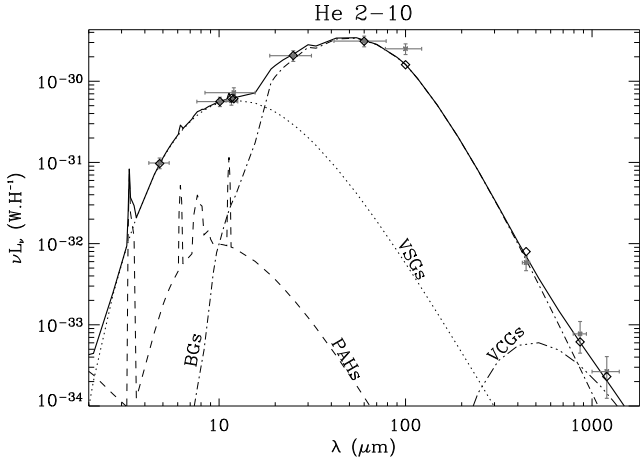
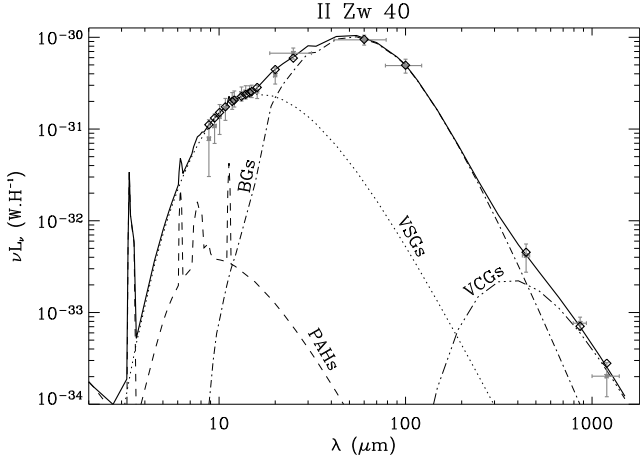


Fig. 3. II Zw 40, He 2-10 and NGC 1140 observations and modeled SED. The data (Table 4) are indicated by crosses: vertical bars are the errors on the flux values and the horizontal bars indicate the widths of the broadbands. The lines are the dust model and the different dust components. Diamonds are the model integrated over the observational broadbands and color-corrected. Thus, departures from the model lie where the diamonds deviate from the crosses. The power is expressed in $W H^{-1}$ which is νL_ν divided by the number of H atoms (L_ν is the monochromatic luminosity).

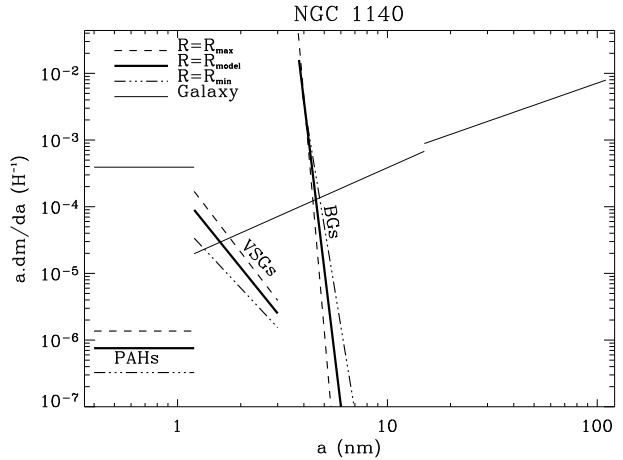
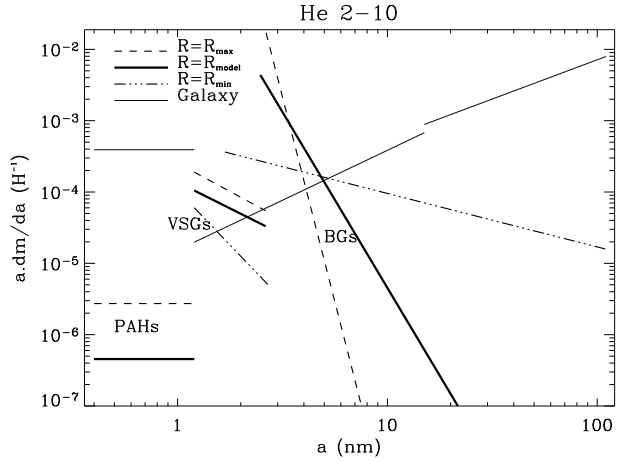
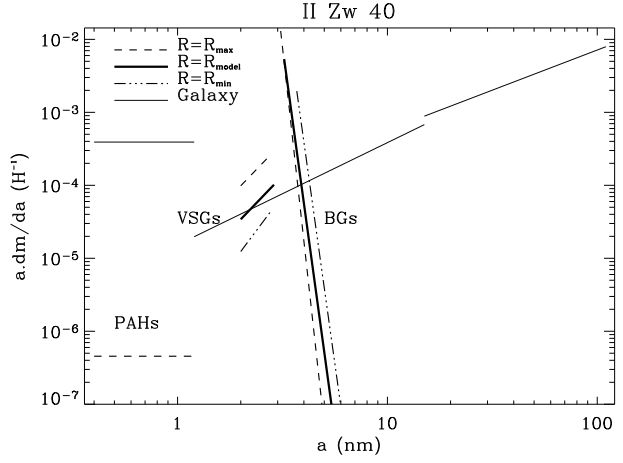


Fig. 4. Size distribution deduced for II Zw 40, He 2-10 and NGC 1140. The solid thick lines are the best fit solution and the non-solid lines are the solutions for the two extreme values of the radius. The grey thin line is the size distribution for our Galaxy (DBP90).

waves following the starburst, as suggested here, could be the main process determining the extinction properties, rather than a deficit in formation of large grains by evolved stars. This argument is also supported by the fact that observations toward some lines of sight in the

SMC show Galactic type extinction (Gordon & Clayton 1998; Gordon et al. 2003) and observations toward some lines of sight inside the Galaxy show SMC like extinction curves (Valencic et al. 2003).

4.5. The dust masses

Table 9 contains all of the most interesting physical quantities deduced from our modelling. The dust masses are directly deduced from Tables 6 and 7. Table 9 highlights the fact that most of the mass is contained in the VCG component, if we believe that the submillimetre excess is produced by very cold dust. There is a large uncertainty on the mass of this component since its temperature is uncertain. However, our results show that between 40 and 80 % of the dust mass is in the form of VCGs. The rest of the dust mass is dominated by the BGs. The VSGs, while the most numerous particles, contain between 1 and 3 % of the total dust mass. To compute the gas-to-dust mass ratio we assume that $M_{gas} = M(\text{H}_1) + M(\text{H}_2) + M(\text{He})$ and that $M(\text{He}) = 0.25 \times M_{gas}$. The $M(\text{H}_1)$ are taken from table 5 and $M(\text{H}_2)$ are given in the literature: Meier et al. (2001) report $M(\text{H}_2) < 0.4 \times 10^6 \text{ M}_\odot$ for II Zw 40 and $M(\text{H}_2) = 1.4 \times 10^8 \text{ M}_\odot$ for He 2-10. For NGC 1140, we assume that $M(\text{H}_2)$ is negligible compared to $M(\text{H}_1)$, since we did not find any global estimate in the literature and this mass is likely to be small. We use the following definition of the dust-to-metal mass ratio: $\mathcal{D} = 1/\mathcal{G}Z$, which is the fraction of metals locked up in dust. The Galactic values are typically $\mathcal{G} \simeq 150$ and $\mathcal{D} \simeq 1/3$. The range of values we give for \mathcal{G} and \mathcal{D} are rather large (Table 9). The constraints that we put on this parameter allows lower values of the dust-to-metal mass ratio than established by other studies (Lisenfeld & Ferrara 1998). The dust-to-metal ratio for the dwarf galaxies may be lower than that of the Milky Way, except for the upper limit of II Zw 40. It would suggest that low-metallicity systems could be less efficient in forming dust than normal metallicity galaxies.

He 2-10 is a special case, since the VCG mass we computed is affected by the fact that the upper limit of the free-free emission we subtracted from the millimetre fluxes in order to be conservative, is significant, and also, since its metallicity is relatively uncertain. This is the reason why the value of \mathcal{D} in He 2-10 deviates from the others.

4.6. The nature of the very cold grain component (VCGs)

In paper II, we discussed the likeliness of the VCG hypothesis by estimating order of magnitudes of the temperature and the filling factor of dust hidden in very dense clumps. Here, we do the same calculation for II Zw 40, He 2-10 and NGC 1140.

Following the equation (11), in paper II, we compute a rough estimate of the temperatures of the VCGs, T_{VCG} . This is the temperature that would be reached by grains totally shielded from the stellar radiation, heated only by

the emission from the surrounding dust. It is estimated assuming that the inferred mass of VCGs will be heated only by the radiation arising from the dust peaking in the FIR in our synthesised SEDs. The ranges of values that we calculate are: $T_{VCG} \simeq 7 - 9 \text{ K}$ for II Zw 40, $T_{VCG} \simeq 8 - 10 \text{ K}$ for He 2-10 and $T_{VCG} \simeq 6 - 9 \text{ K}$ for NGC 1140. All these values are consistent with the temperatures given in Table 6 except in the case of He 2-10 where the high level of the upper limit of the free-free emission gives more uncertainty on the VCG parameters. We believe that these figures support the hypothesis of very cold dust in dense clumps to explain the submm excess of the SEDs.

We are also able to give an idea of the size of the clumps and of their filling factor. As we did in paper II, for NGC 1569, we assume that the BGs are shielding the VCGs. If we assume typical contrast densities of $\delta = 10^4 - 10^5$, we find clump sizes of $0.9 - 18 \text{ pc}$ for II Zw 40, $1.2 - 38 \text{ pc}$ for He 2-10 and $2.4 - 43 \text{ pc}$ for NGC 1140. The corresponding filling factors are: $2 \times 10^{-4} - 2 \times 10^{-3}$ for II Zw 40, $3 \times 10^{-4} - 3 \times 10^{-3}$ for He 2-10 and $4 \times 10^{-5} - 8 \times 10^{-4}$ for NGC 1140. Thus, our conclusion is that the ISM of these galaxies could be very clumpy with low filling factors. In contrast, the filling factor of the Galactic molecular phase is about 1 % (Tielens 1995). Recently, André et al. (2004), found very small ($\simeq 100 \text{ pc}$) dense CO clumps in the low-metallicity ISM of the Magellanic clouds. These clumps could contain the very cold dust probed by our submm-mm SEDs. Rubio et al. (2004) found that the CO mass deduced from the submillimeter continuum emission of molecular cloud in the SMC, is ~ 10 times higher than the virial mass reported from CO observations. Their interpretation is that the CO emission comes from dense clumps.

5. Summary and conclusion

We have presented new SCUBA images at $450 \mu\text{m}$ and $850 \mu\text{m}$ and MAMBO ON-OFF observations of II Zw 40, He 2-10 and NGC 1140. With additional data from the literature, we have constructed the observed SEDs for these galaxies. Using the same modelling approach as in paper II, we have combined stellar evolution, photoionisation and dust modelling to compute self-consistent dust SEDs. The results found in paper II, for NGC 1569, are supported here, for II Zw 40, He 2-10 and NGC 1140.

1. We find very low abundances of PAHs, and smaller overall sizes ($\sim 3 - 4 \text{ nm}$) of grains emitting in the mid-IR and far-IR, in contrast to grains observed in the Galaxy. The small sizes of the grains, on average, are supported by the erosion by shock waves produced by the numerous supernovae that occurred in these starburst galaxies.
2. Due to the small sizes of the grains, the stochastic heating of dust is predominant in these galaxies, even the grains emitting at far-IR wavelengths. The bulk of the emission comes from grains which are not in thermal equilibrium with the radiation field.

	NGC 1569	II Zw 40	He 2-10	NGC 1140
L_{dust} (L_{\odot})	$(5.8 \pm 0.1) \times 10^8$	$(2.0 \pm 0.2) \times 10^9$	$(5.4 \pm 0.2) \times 10^9$	$(3.3 \pm 0.1) \times 10^9$
L_{\star}^{ext} (L_{\odot})	$(1.3 \pm 0.1) \times 10^9$	$(2.5 \pm 0.1) \times 10^9$	$(5.3 \pm 0.2) \times 10^9$	$(6.0 \pm 0.2) \times 10^9$
τ_V^{eff}	0.24	0.15	0.26	0.11
M_{PAH} (M_{\odot})	$\lesssim 190$	$\lesssim 220$	$\lesssim 930$	$6.2_{-2.5}^{+4.2} \times 10^3$
M_{VSG} (M_{\odot})	$3.4_{-0.9}^{+1.0} \times 10^3$	$1.0_{-0.4}^{+0.7} \times 10^4$	$1.5_{-0.7}^{+0.8} \times 10^4$	$1.7_{-0.4}^{+0.9} \times 10^5$
M_{BG} (M_{\odot})	$8.4_{-1.7}^{+0.5} \times 10^4$	$1.1_{-0.3}^{+0.6} \times 10^5$	$2.8_{-1.2}^{+1.9} \times 10^5$	$4.6_{-2.0}^{+2.3} \times 10^6$
M_{VCG} (M_{\odot})	$(0.7 - 2.5) \times 10^5$	$(3.1 - 8.8) \times 10^5$	$(0.2 - 1.3) \times 10^6$	$(0.2 - 1.3) \times 10^7$
Total M_d (M_{\odot})	$(1.6 - 3.4) \times 10^5$	$(0.4 - 1.1) \times 10^6$	$(0.4 - 1.8) \times 10^6$	$(0.5 - 2.0) \times 10^7$
\mathcal{G}	740 – 1600	530 – 1460	330 – 1500	500 – 2000
\mathcal{D}	1/6 – 1/3	1/5 – 1/2	1/30 – 1/6	1/13 – 1/3

Table 9. Derived quantities from our dust modelling, for NGC 1569 (paper II), II Zw 40, He 2-10 and NGC 1140. L_{dust} is the luminosity reemitted by the dust from near-IR to mm. L_{\star}^{ext} is the escaping stellar luminosity. τ_V^{eff} is the effective optical depth deduced from the energy balance (see paper II). M_{PAH} , M_{VSG} , M_{BG} and M_{VCG} are the masses of each dust component and M_d is the total dust mass. \mathcal{G} is the gas-to-dust mass ratio and \mathcal{D} is the dust-to-metal mass ratio. The Galactic values are typically $\mathcal{G} \simeq 150$ and $\mathcal{D} \simeq 1/3$.

3. In each of our four SEDs presented here and in paper II, we find, with no exception, a submillimetre emission excess. We propose that this excess is the emission of very cold dust ($5 \text{ K} \lesssim T \lesssim 9 \text{ K}$) hidden in dense clumps. In each of these SEDs, except one, we find that $\beta = 1$ is the most likely value for the emissivity index of this component, even if this parameter is difficult to accurately constrain with the scarcity of data in the submillimetre-millimetre part of the spectra. Very cold grains represent between 40 and 80 % of the total dust mass. We show that this very cold dust hypothesis is consistent, although we can not exclude other explanations for this millimetre excess, like non-standard optical properties.
4. The submillimetre-millimetre emission is not concentrated toward the outer regions of the galaxies but correlated with the mid-IR emission distributed around the star forming regions. Our results are consistent with a clumpy medium composed of ubiquitous clumps of sizes between a few pc to a few tens of pc with typical filling factor of $10^{-4} - 10^{-3}$.
5. The extinction curves that we synthesize for the 4 dwarf galaxies are different from that of the Galaxy and similar in shape to that of the LMC. Due to the small sizes of the grains and the low abundance of PAHs (or lack of PAHs), the slope of the extinction curves are constant from near-IR to far-UV wavelengths with the greatest extinction in the UV range. The extinction bump at 2175 Å, which is assumed to be carried by the very small grains in the dust model we use, is found to be smaller than the Galactic one in our sample except in one case where we have a high mid-IR attenuation.
6. We constrain the gas-to-dust mass ratios which lie between 300 and 2000 and the dust-to-metal mass ratios which lie between 1/30 and 1/2 in our sample.

This paper closes a serie of three publications related to the MIR to mm properties of low-metallicity environments. This study investigates the dust properties of 3 new

low-metallicity galaxies, II Zw 40, He 2-10 and NGC 1140 and along with NGC 1569 (paper II), presents the first detailed SED studies focused on dwarf galaxies. The study of dust properties using IR emission provides results that are overlooked by optical studies based on the extinction phenomenon. Dust properties are profoundly different in these galaxies compared to our Galaxy and other normal galaxies. The dust size distribution is different, consequently the SEDs and the extinction laws are not the same. Moreover the dust mass and temperature estimates are affected by both the presence of very cold dust and by the non-thermal equilibrium heating of the bulk of the emitting dust. Assuming Galactic dust properties when looking at these galaxies is not correct and could lead to large errors, particularly in dust masses.

We also warn the reader that it is very important to obtain data in the MIR regime as well as in the submillimetre/millimetre regime to properly constrain the dust properties. The submillimetre/millimetre regime is still largely unknown and poorly sampled. Observations of galaxies at these wavelengths could contribute significantly to the comprehension of the variety of galactic dust environments. Without such precise dust SED modeling incorporating the submillimetre/millimetre wavelength range, inaccurate results could lead to poor assumptions in galaxy number counts and galaxy evolution models. The future ground-based, airborne and space observatories exploring the FIR to millimetre wavelength regime, such as SOFIA, ASTRO-F, Herschel, Planck and ALMA hold great expectations in the investigation of extragalactic dust properties and will bring us many steps closer of the understanding of the physics of the ISM of galaxies.

Acknowledgements. We would like to thank René Gastaud, Hélène Roussel, Pierre Chanial and Marc Sauvage for their expert advice on ISOCAM data reduction; Andrew Baker, Thomas Stanke and Ute Lisenfeld for their assistance at IRAM radio-telescope and their help on data reduction and Axel Weiss and Frank Bertoldi for their technical help; Marc Sauvage, who provided us his M band image of He 2-10 in advance of publication; Leonardo Vanzi for his near-IR images

of II Zw 40; Laurent Verstraete, who provided us his updated model of the PAH emission in the DBP90 model; Jean-Luc Starck, for useful discussion on data processing techniques. We also thank Ute Lisenfeld and Frank Israel for helpful scientific discussion. We are very grateful to François Boulanger and Eli Dwek for invaluable insight on this subject which improved the scientific quality of the paper. Finally, we thank the referee for his report, especially for his suggestion to consider the Akaike's Information Criterion.

Appendix A: Degeneracies in dust modelling

In this appendix, we demonstrate a well-known degeneracy between the energy source, and the grain properties, which must be considered when modelling a dust SED.

The dust SED of a given region depends *(i)* on the optical properties of the different types of grains, *(ii)* on the size distribution of these grains and *(iii)* on the shape and the intensity of the heating radiation field.

Optical properties of the grains are based on laboratory experiments and astrophysical measurements, it is not relevant to vary them in order to fit an observed SED. However, the radiation field depends on the environment. The grains will experience a different radiation field in a starburst region than in the diffuse ISM. The top-left plot of Fig. A.1 shows the fit of a fake observed SED (the grey crosses) with the Désert et al. (1990) model by varying the ISRF but keeping the Galactic grain size distribution. The radiation field needed to fit this SED is the grey line on the bottom-left plot on Fig. A.1, compared to the Galactic one, in black.

The dust size distribution is also a set of parameters varying significantly in different environments. Indeed, it is subject to fragmentation and erosion by shock waves, evaporation near strong radiation sources, or coagulation and accretion of material in dense media. The top-right plot of Fig. A.1 shows the same fake observed SED than on the top-left plot, but fitted with the Désert et al. (1990) model by varying the size distribution and keeping the Galactic radiation field. We get a good fit, in this case, too. The bottom-right plot of Fig. A.1 shows the required size distribution to fit the SED, in grey, compared to the Galactic one, in black.

These two examples show that, without caution, we can interpret the same SED with two different physical solutions. We emphasize the need to constrain both the ISRF and the size distribution when modelling a dust SED. Our modelling approach was aimed to achieve that goal.

Appendix B: Peculiar optical properties to explain the submillimeter excess

Agladze et al. (1996) measured the variation of the emissivity index, β , of various silicate and carbonaceous materials with the temperature (Fig. B.1). We have implemented their observations in order to explain the submillimeter excess of our SEDs.

We modified the optical properties of the BGs, by constructing a temperature dependent absorption efficiency $Q_{\text{abs}}(\lambda, a, T)$ (Fig. B.2). In the standard DBP90 model, the BGs are silicate grains and have an index $\beta = 2$, in the submillimeter regime. The amorphous MgSiO_3 and Mg_2SiO_4 are the two species studied by Agladze et al. (1996) which are consistent with the BGs. This modification can have a significant effect, if the contribution by cold BGs ($T_{\text{BG}} \lesssim 25$ K) is important.

For a given grain size, cold BGs can exist due to temperature fluctuations. They cool down between two photon absorptions. In our case, the monochromatic luminosity emitted by a BG of radius a is:

$$\mathcal{L}_\lambda(\lambda, a) = \int_0^\infty 4\pi B_\lambda(\lambda, T) \pi a^2 Q_{\text{abs}}(\lambda, a, T) \frac{dP}{dT} dT, \quad (\text{B.1})$$

where $B_\lambda(\lambda, T)$ is the Planck function, and dP/dT the temperature distribution. Otherwise, BGs can be cold if they are large enough. The total luminosity emitted by the BGs, with the number size distribution $f(a)$, is:

$$L_\lambda(\lambda) = \int_0^\infty \mathcal{L}_\lambda(\lambda, a) f(a) da. \quad (\text{B.2})$$

Among our four dwarf galaxies, the only detectable effect of these peculiar optical properties can be seen in NGC 1569 (Fig. B.3). For the three other SEDs, the two models give identical results.

Finally, we conclude that this effect is not able to reproduce the submillimeter excess. This does not mean that we can exclude other peculiar, as yet unexplored, optical properties to explain this excess.

References

Agladze, N. I., Sievers, A. J., Jones, S. A., Burlitch, J. M., & Beckwith, S. V. W. 1996, *ApJ*, 462, 1026
 Allen, D. A., Wright, A. E., & Goss, W. M. 1976, *MNRAS*, 177, 91
 André, M. K., Le Petit, F., Sonnentrucker, P., et al. 2004, *A&A*, 422, 483
 Baas, F., Israel, F. P., & Koornneef, J. 1994, *A&A*, 284, 403
 Beck, S. C., Kelly, D. M., & Lacy, J. H. 1997, *AJ*, 114, 585
 Beck, S. C., Turner, J. L., Langland-Shula, L. E., et al. 2002, *AJ*, 124
 Bot, C., Boulanger, F., Lagache, G., & Cambrésy, L. 2004, *A&A*
 Brinks, E. & Klein, U. 1988, *MNRAS*, 231, 63P
 Broguière, D., Neri, R., Sievers, A., & Wiesemeyer, H. 2002, NIC. Bolometer Users Guide, Tech. rep., IRAM
 Buat, V., Burgarella, D., Deharveng, J. M., & Kunth, D. 2002, *A&A*, 393, 33
 Cairós, L. M., Vílchez, J. M., González Pérez, J. N., Iglesias-Páramo, J., & Caon, N. 2001, *ApJS*, 133, 321
 Condon, J. J. 1992, *ARA&A*, 30, 575

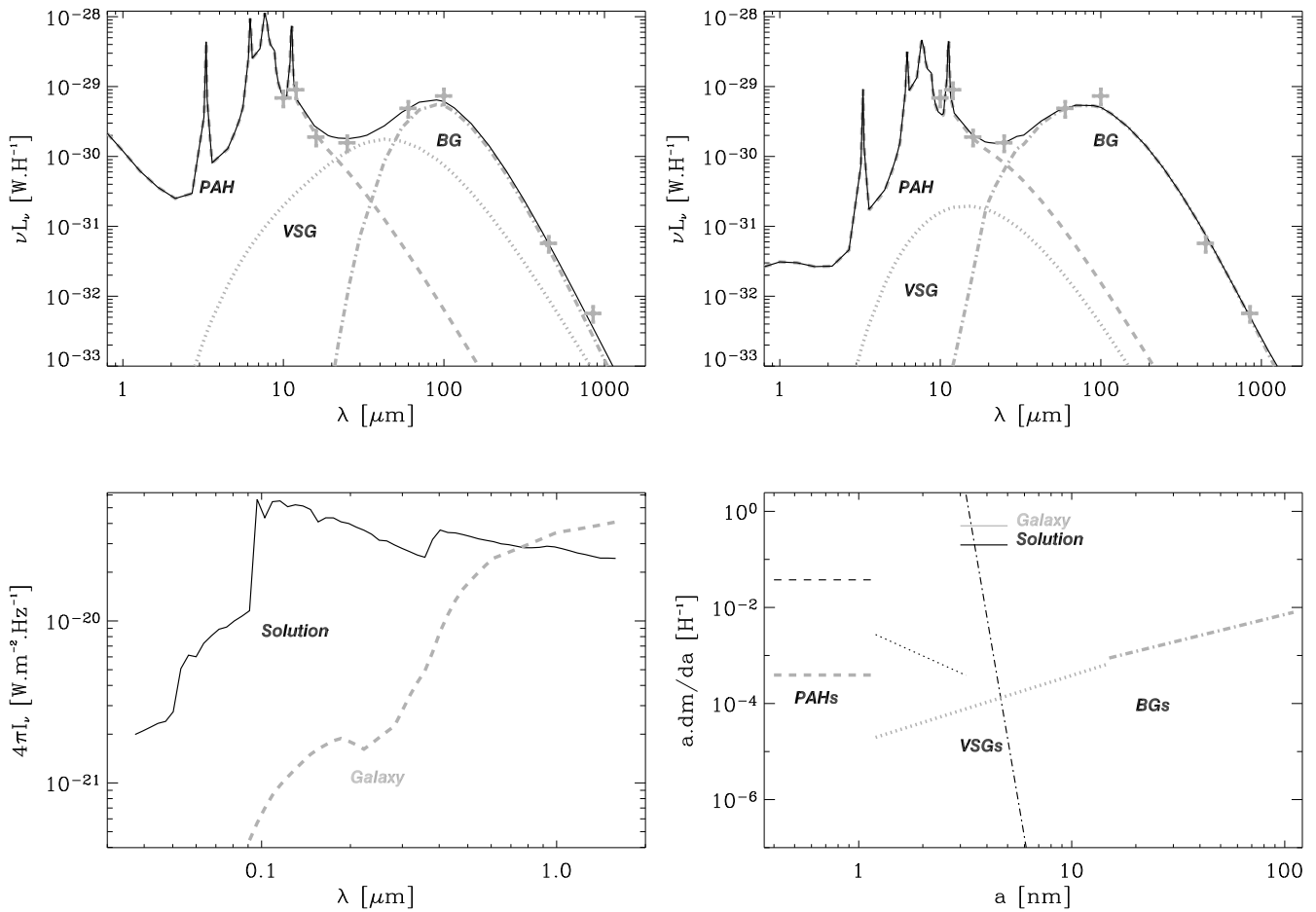


Fig. A.1. The two top plots show the same fake observed dust SED (the grey crosses) fitted with the DBP90 model by varying two different sets of parameters. The top-left plot has been fitted by varying the radiation field and keeping the Galactic size distribution. The top-right plot has been fitted by varying the size distribution and keeping the Galactic radiation field. The bottom-left plot shows the radiation field required for the top-left plot, compared to the Galactic one. The bottom-right plot shows the size distribution required for the top-right plot, compared to the Galactic one.

Conti, P. S. 1991, ApJ, 377, 115
 de Grijs, R., Smith, L. J., Bunker, A., et al. 2004, MNRAS, 352, 263
 de Vaucouleurs, G., de Vaucouleurs, A., Corwin, H. G., et al. 1991, Third Reference Catalogue of Bright Galaxies (Volume 1-3, XII, 2069 pp. 7 figs.. Springer-Verlag Berlin Heidelberg New York)
 Deeg, H.-J., Duric, N., & Brinks, E. 1997, A&A, 323, 323
 Désert, F.-X., Boulanger, F., & Puget, J.-L. 1990, A&A, 237, 215
 Draine, B. T. & Li, A. 2001, ApJ, 551, 807
 Ferland, G. J. 1996, HAZY, a brief introduction to CLOUDY, Tech. rep., University of Kentucky, department of physics and astronomy
 Fioc, M. & Rocca-Volmerange, B. 1997, A&A, 326, 950
 Gallagher, J. S. & Hunter, D. A. 1987, AJ, 94, 43
 Galliano, F. 2005, in "The Spectral Energy Distribution of Gas-Rich Galaxies: Confronting Models with Data", Heidelberg, 4-8 Oct. 2004, eds. C.C. Popescu & R.J.

Tuffs, AIP Conf. Ser., in press
 Galliano, F., Madden, S., Jones, A. P., et al. 2002, in EAS Publications Series, Volume 4, Proceedings of Infrared and Submillimeter Space Astronomy", held 11-13 June, 2001. Edited by M. Giard, J.P. Bernard, A. Klotz, and I. Ristorcelli. EDP Sciences, 2002, pp.381-385, Vol. 4, 381-385
 Galliano, F., Madden, S. C., Jones, A. P., et al. 2003, A&A, 407, 159
 Gordon, K. D. & Clayton, G. C. 1998, ApJ, 500, 816
 Gordon, K. D., Clayton, G. C., Misselt, K. A., Landolt, A. U., & Wolff, M. J. 2003, ApJ, 594, 279
 Guseva, N. G., Izotov, Y. I., & Thuan, T. X. 2000, ApJ, 531, 776
 Heckman, T. M., Robert, C., Leitherer, C., Garnett, D. R., & van der Rydt, F. 1998, ApJ, 503, 646
 Heisler, C. A. & Vader, J. P. 1994, AJ, 107, 35
 Holland, W. S., Robson, E. I., Gear, W. K., et al. 1999, MNRAS, 303, 659

Hunter, D. A. & Gallagher, J. S. 1985, AJ, 90, 1457

Hunter, D. A., Gallagher, J. S., Rice, W. L., & Gillett, F. C. 1989, ApJ, 336, 152

Hunter, D. A., O'Connell, R. W., & Gallagher, J. S. 1994a, AJ, 108, 84

Hunter, D. A. & Sage, L. 1993, PASP, 105, 374

Hunter, D. A., van Woerden, H., & Gallagher, J. S. 1994b, ApJS, 91, 79

Ivezic, Z. & Elitzur, M. 1997, MNRAS, 287, 799

Joblin, C., Leger, A., & Martin, P. 1992, ApJ, 393, L79

Johansson, I. 1987, A&A, 182, 179

Johnson, K. E., Leitherer, C., Vacca, W. D., & Conti, P. S. 2000, AJ, 120, 1273

Jones, A. P., Tielens, A. G. G. M., & Hollenbach, D. J. 1996, ApJ, 469, 740

Kinney, A. L., Bohlin, R. C., Calzetti, D., Panagia, N., & Wyse, R. F. G. 1993, ApJS, 86, 5

Klein, U., Graeve, R., & Wielebinski, R. 1983, A&A, 117, 332

Kobulnicky, H. A., Dickey, J. M., Sargent, A. I., Hogg, D. E., & Conti, P. S. 1995, AJ, 110, 116

Kobulnicky, H. A. & Johnson, K. E. 1999, ApJ, 527, 154

Kobulnicky, H. A., Kennicutt, R. C., & Pizagno, J. L. 1999, ApJ, 514, 544

Koornneef, J. & Code, A. D. 1981, ApJ, 247, 860

Kreysa, E., Gemünd, H.-P., & Gromke, J., e. a. 1999, Infrared Physics & Technology, 40, 191

Le Borgne, D., Rocca-Volmerange, B., Prugniel, P., et al. 2004, A&A, 425, 881

Li, A. & Draine, B. T. 2001, ApJ, 554, 778

Lisenfeld, U. & Ferrara, A. 1998, ApJ, 496, 145

Lisenfeld, U., Israel, F. P., Stil, J. M., & Sievers, A. 2002, A&A, 382, 860

Méndez, D. I., Esteban, C., Filipović, M. D., et al. 1999, A&A, 349, 801

Madden, S. C. 2000, New Astronomy Review, 44, 249

Madden, S. C., Galliano, F., Jones, A. P., & Sauvage, M. 2005, A&A, *to be submitted*

Maiolino, R., Marconi, A., & Oliva, E. 2001a, A&A, 365, 37

Maiolino, R., Marconi, A., Salvati, M., et al. 2001b, A&A, 365, 28

Martín-Hernández, N. L., Schaefer, D., & Sauvage, M. 2005, *in preparation*

Mas-Hesse, J. M. & Kunth, D. 1999, A&A, 349, 765

Masegosa, J., Moles, M., & Campos-Aguilar, A. 1994, ApJ, 420, 576

Meier, D. S., Turner, J. L., Crosthwaite, L. P., & Beck, S. C. 2001, AJ, 121, 740

Melisse, J. P. M. & Israel, F. P. 1994, A&AS, 103, 391

Nandy, K., Morgan, D. H., Willis, A. J., Wilson, R., & Gondhalekar, P. M. 1981, MNRAS, 196, 955

Plante, S. & Sauvage, M. 2002, AJ, 124, 1995

Prévot, M. L., Lequeux, J., Prévot, L., Maurice, E., & Rocca-Volmerange, B. 1984, A&A, 132, 389

Roche, P. F., Aitken, D. K., Smith, C. H., & Ward, M. J. 1991, MNRAS, 248, 606

Rubio, M., Boulanger, F., Rantakyro, F., & Contursi, A. 2004, A&A, 425, L1

Sage, L. J., Salzer, J. J., Loose, H.-H., & Henkel, C. 1992, A&A, 265, 19

Saikia, D. J., Pedlar, A., Unger, S. W., & Axon, D. J. 1994, MNRAS, 270, 46

Sauvage, M., Thuan, T. X., & Lagage, P.-O. 1997, A&A, 325, 98

Sauvage, M. & Vanzi, L. 2005, *in preparation*

Savage, B. D. & Mathis, J. S. 1979, ARA&A, 17, 73

Sramek, R. A. & Weedman, D. W. 1986, ApJ, 302, 640

Starck, J.-L., Murtagh, F., & Bijaoui, A. 1998, Image processing and data analysis: the multiscale approach (Cambridge University Press)

Takeuchi, T. T. 2000, Ap&SS, 271, 213

Takeuchi, T. T., Hirashita, H., Ishii, T. T., Hunt, L. K., & Ferrara, A. 2003, MNRAS, 343, 839

Takeuchi, T. T., Yoshikawa, K., & Ishii, T. T. 2000, ApJS, 129, 1

Telesco, C. M., Dressel, L. L., & Wolstencroft, R. D. 1993, ApJ, 414, 120

Thronson, H. A. & Telesco, C. M. 1986, ApJ, 311, 98

Thuan, T. X., Sauvage, M., & Madden, S. 1999, ApJ, 516, 783

Tielens, A. G. G. M. 1995, in ASP Conf. Ser. 73: From Gas to Stars to Dust, 3–22

Vacca, W. D. & Conti, P. S. 1992, ApJ, 401, 543

Vacca, W. D., Johnson, K. E., & Conti, P. S. 2002, AJ, 123, 772

Valencic, L. A., Clayton, G. C., Gordon, K. D., & Smith, T. L. 2003, ApJ, 598, 369

van Zee, L., Skillman, E. D., & Salzer, J. J. 1998, AJ, 116, 1186

Vanzi, L., Rieke, G. H., Martin, C. L., & Shields, J. C. 1996, ApJ, 466, 150

Vanzi, L. & Sauvage, M. 2004, A&A, 415, 509

Walsh, J. R. & Roy, J. 1993, MNRAS, 262, 27

Weingartner, J. C. & Draine, B. T. 2001, ApJ, 548, 296

Wild, W. 1999, A handbook for the IRAM 30m telescope, Tech. rep., IRAM, Pico-Veleta, Spain

Zubko, V., Dwek, E., & Arendt, R. G. 2004, ApJS, 152, 211

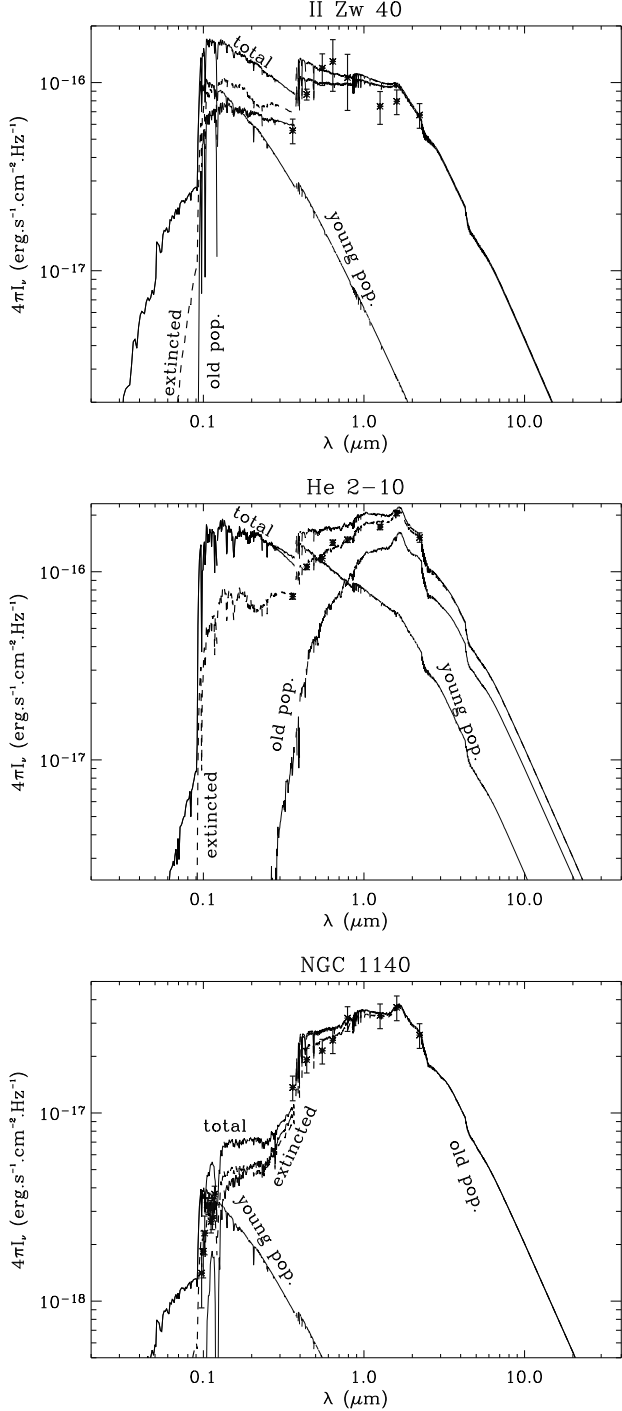


Fig. 5. Synthesized ISRFs for II Zw 40, He 2-10 and NGC 1140 computed with PÉGASE and CLOUDY. The points with error bars are the observational data from Table 3, the solid black line is the global non-extincted ISRF, the dashed line is the global extincted ISRF and the grey line is the young single-burst component. The extinction curve used is the output from the dust model DBP90.

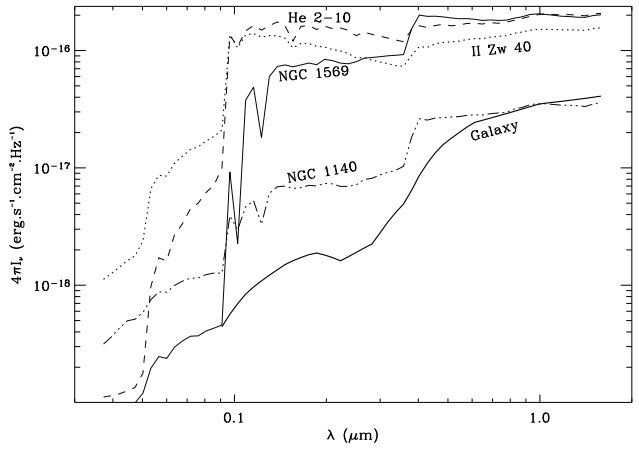


Fig. 6. Comparison of the synthesized ISRFs of NGC 1569 (paper II), II Zw 40, He 2-10 and NGC 1140, with the Galactic one (DBP90). These ISRFs are the effective radiation fields seen by the dust in our model.

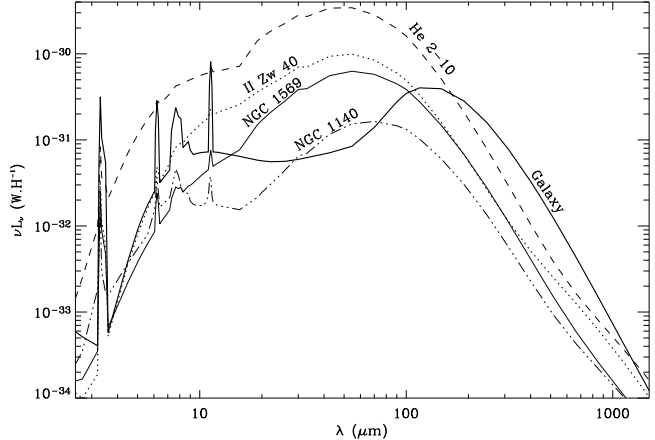


Fig. 7. Comparison of the modeled dust SEDs of NGC 1569 (paper II), II Zw 40, He 2-10 and NGC 1140 (this paper), and that of the Galaxy (DBP90).

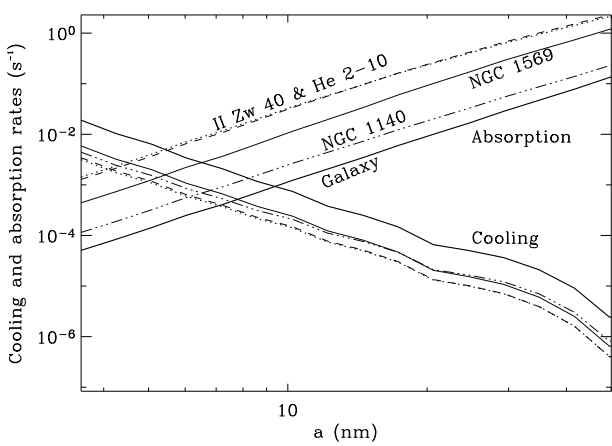


Fig. 8. Cooling rates and photon absorption rates as a function of the grain radius a for NGC 1569, II Zw 40, He 2-10 and NGC 1140, compared to the Galaxy.

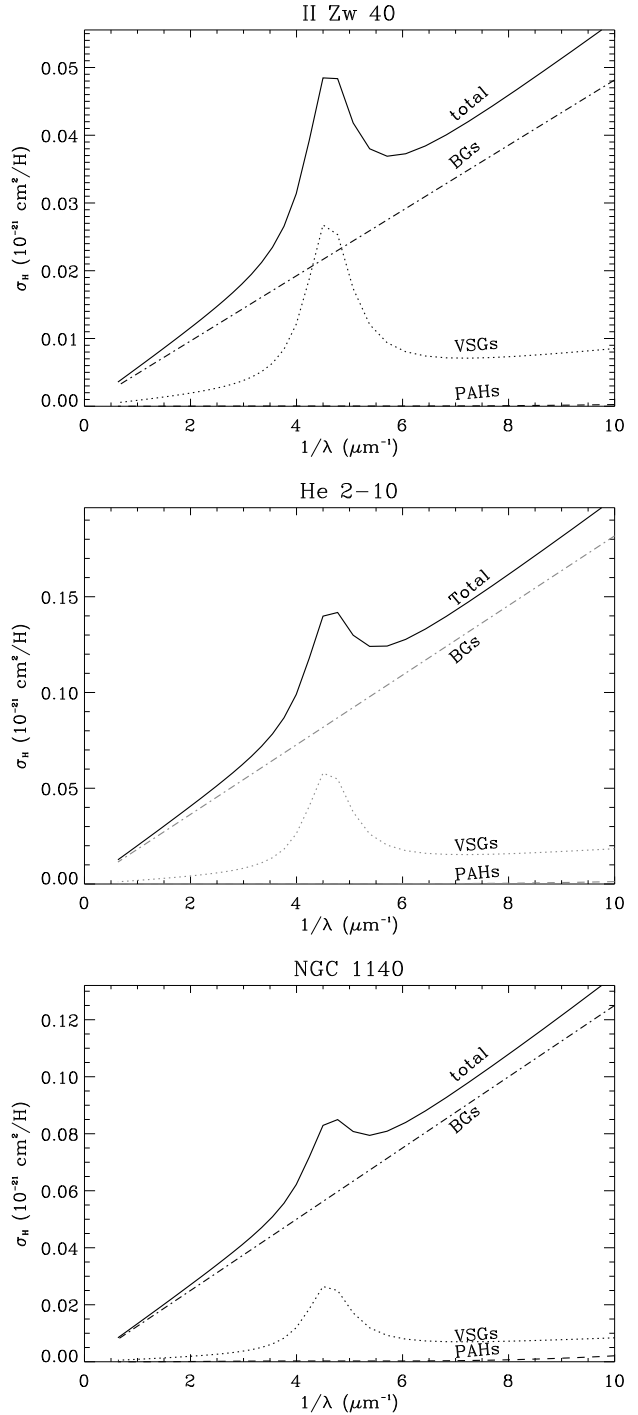


Fig. 9. Synthesized extinction curves for II Zw 40, He 2-10 and NGC 1140. The contributions to the extinction are shown individually for the PAH, VSG and BG components. The solid lines are the total extinction curves modeled with DBP90. The opacity is expressed as the cross section per H atom.

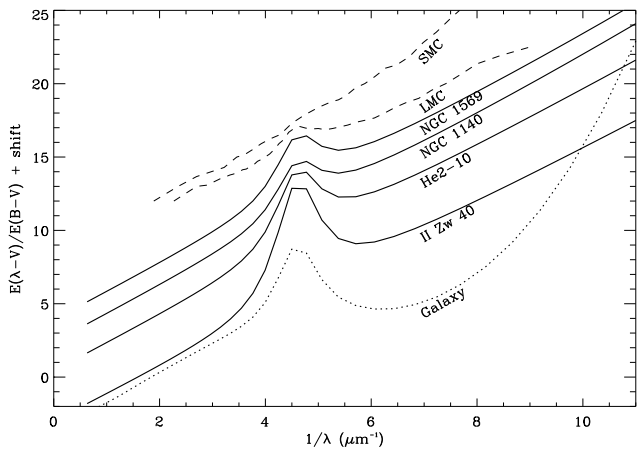


Fig. 10. Comparison of the synthesized extinction curves of NGC 1569 (paper II), II Zw 40, He 2-10 and NGC 1140 with the Galactic extinction curve (DBP90), the observed LMC curve (average of Koornneef & Code (1981) and Nandy et al. (1981)) and the observed SMC curve (Prévôt et al. 1984). These curves have been shifted for clarity.

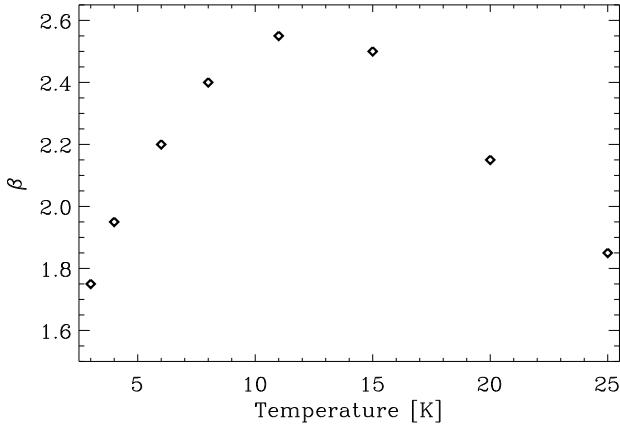


Fig. B.1. Variation of the emissivity index, β , as a function of the temperature, T , for Mg_2SiO_4 , as measured by Agladze et al. (1996).

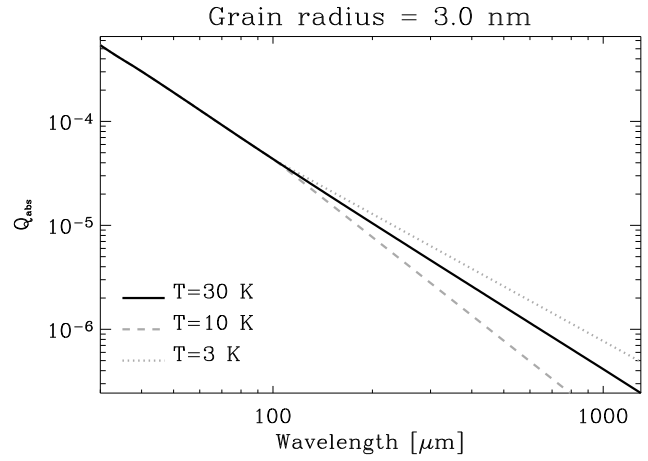


Fig. B.2. Modification of the optical properties of the BGs, following the measurements by Agladze et al. (1996) shown in Fig. B.1.

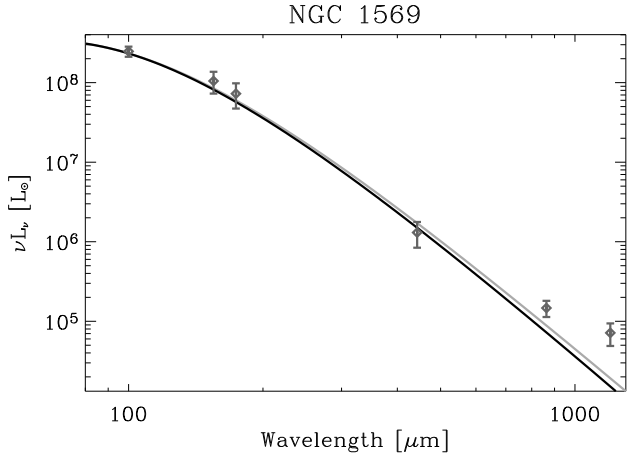


Fig. B.3. Fit of the long wavelength SED of NGC 1569 (paper II), with the standard model (in black), and with the modified optical properties (in grey), using the temperature dependent Q_{abs} .